JOURNAL OF GEOPHYSICAL RESEARCH, VOL. 104, NO. C4, PAGES 7785–7806, APRIL 15, 1999

Heat budget of snow-covered sea ice at North Pole 4

Rachel E. Jordan and Edgar L Andreas
U.S. Army Cold Regions Research and Engineering Laboratory, Hanover, New Hampshire

Aleksandr P. Makshtas
Arctic and Antarctic Research Institute, St. Petersburg, Russia

Abstract. The Russian drifting station North Pole 4 (NP-4) was within 5° latitude of the North Pole from April 1956 to April 1957. We use a wide-ranging set of snow and meteorological data collected at 3-hourly intervals on NP-4 during this period to investigate energy and mass transfer in the snow, sea ice, and atmospheric surface layer in the central Arctic. SNTHERM, a one-dimensional energy and mass balance model, synthesizes these diverse NP-4 data and thereby yields energetically consistent time series of the components of the surface heat budget. To parameterize the sensible heat flux during extremely stable stratification, we replace the usual log-linear stability function with the "Dutch" formulation and introduce a windless coefficient in the bulk parameterization. This coefficient provides sensible heat transfer at the surface, even when the mean wind speed is near zero, and thereby prevents the surface temperature from falling to unrealistically low values, a common modeling problem when the stratification is very stable. Several other modifications to SNTHERM introduce procedures for creating a realistic snowpack that has continuously variable density and is subject to erosion and wind packing. The NP-4 data provide for two distinct simulations: one on 2-year ice and one on multiyear ice. We validate our modeling by comparing simulated and observed temperatures at various depths in the snow and sea ice. Simulations for both sites show the same tendencies. During the summer, the shortwave radiation is the main term in the surface heat budget. Shortwave radiation also penetrates into the snow and causes a subsurface temperature maximum that both the data and the model capture. During the winter, the net longwave balance is the main term in the surface heat budget. The snow and sea ice cool in response to longwave losses, but the flux of sensible heat from the air to the surface mitigates these losses and is thus nearly a mirror image of the emitted longwave flux.

1. Introduction and Background

Much of what we know about the turbulent and radiative fluxes at the surface of the Arctic Ocean has come from observations on the 31 Russian "North Pole" (NP) drifting stations that plied the Arctic in 1937, 1950–1951, then continuously during 1952–1991. Rarely, however, have western scientists been able to see the raw data from the NP stations. Rather, our information has come from the highly processed charts and tables in the famous Russian atlases and in comparable syntheses [*Fletcher et al.*, 1966; *Gorshkov*, 1983; *Treshnikov*, 1985; *Marshunova*, 1961; *Chernigovskii and Marshunova*, 1965; *Marshunova and Mishin*, 1994].

Published analyses of data from the early NP stations [e.g., *Yakovlev*, 1958; *Bespalov*, 1959; *Laikhtman*, 1959; *Doronin*, 1963, 1966; *Nazintsev*, 1964], however, give some insights into the theory and data manipulations that went into preparing these meteorological fields. In particular, we see that estimates of the turbulent surface fluxes were derived without the benefit of Monin-Obukhov similarity theory (MOST) [*Monin and Obukhov*, 1954], whose exposition coincided roughly with the deployment of NP-4. MOST was thus in its infancy during these early analyses. In fact, it would be 15 years before the Kansas experiment unequivocally validated the concepts of MOST and thereby confirmed the existence of the empirical similarity functions necessary for analyzing atmospheric surface layer data in the context of the theory [*Businger et al.*, 1971; *Haugen*, 1973; *Dyer*, 1974; *Businger*, 1988; *Kaimal and Wyngaard*, 1990].

The upshot is that these early analyses of data from the NP stations were done before MOST consolidated our understanding of the atmospheric boundary layer. In particular, summary charts of turbulent surface heat fluxes over Arctic sea ice in some of the Russian atlases [e.g., *Gorshkov*, 1983] were prepared without any or only crude accounting for the effects of boundary layer stratification that MOST provides. We know now, however, that unstable stratification enhances turbulent exchange, while stable stratification suppresses it. Consequently, ignoring stratification effects belies the fundamental asymmetry in the magnitudes of the turbulent heat fluxes in stable and unstable conditions.

With the recent relaxing of East-West tension, however, the raw data from the NP stations are now becoming available to western scientists. In fact, the National Snow and Ice Data Center [*NSIDC*, 1996] at the University of Colorado in Boulder, in collaboration with the Applied Physics Laboratory at the University of Washington and the Arctic and Antarctic Research Institue (AARI) in St. Petersburg, Russia, has prepared a CD-ROM, "Arctic Ocean Snow and Meteorological

Paper number 1999JC900011.
0148-0227/99/1999JC900011$09.00

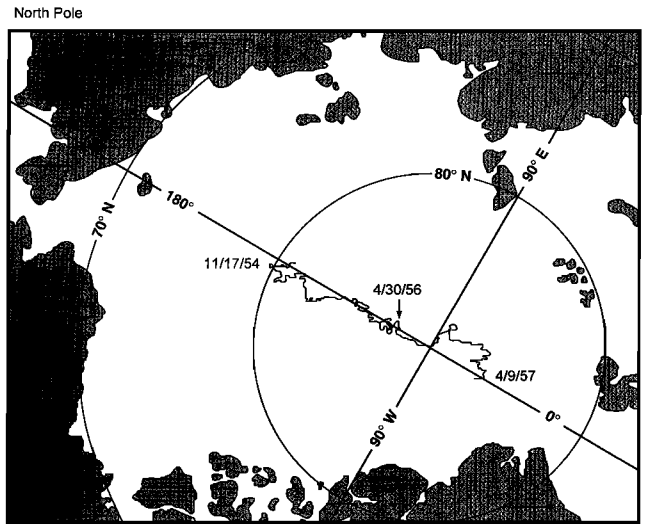

Figure 1. Drift track of North Pole 4. The portion of the drift we consider here is from April 1956, when the station was near 87°N, 180°E, until the end of the drift in April 1957. (Redrawn from *Colony et al.* [1990].)

Observations From Drifting Stations: 1937, 1950–1991, Version 1.0," as part of the Russian-American data rescue program.

We use data on this CD-ROM and other data from the AARI archives, such as temperature profiles in the snow and sea ice, to revisit NP-4 (Figure 1). NP-4 was a special station that warrants our interest for at least three reasons. (1) Objectives on NP-4 included detailed micrometeorological, radiation, and in-snow and in-ice measurements; (2) these observations were continuous for over a year, April 1956 to April 1957; and (3) NP-4 was near the geographical North Pole during this year.

The focus of our NP-4 analysis is the surface heat fluxes and the heat fluxes in the snow and sea ice. While we could compute these for each observation period using the bulk-aerodynamic method for the atmospheric turbulent fluxes and standard conductivity relations for the in-ice and in-snow fluxes, we choose instead to assimilate all the NP-4 data into an internally consistent set of fluxes and processes using SNTHERM. SNTHERM is a one-dimensional mass and energy balance model originally developed for snow-covered ground [*Jordan*, 1991; *Koh and Jordan*, 1995; *Rowe et al.*, 1995] but adapted here for the first time to a sea ice environment.

Part of this adaptation is replacing the standard log-linear formulation with one developed by *Holtslag and de Bruin* [1988] and *Beljaars and Holtslag* [1991]. This latter formulation extends the region of turbulent exchange during stable stratification from a critical Richardson number of 0.2 to 1.43. In addition, we introduce a windless transfer coefficient in the bulk parameterization for the turbulent sensible heat flux. This coefficient allows heat exchange even when the mean wind speed is near zero and therefore prevents the surface temperature from falling to unrealistically low values, a common modeling problem over snow during light winds with strong longwave radiation losses. Other adaptations involve how SNTHERM treats the snow itself. We introduce an algorithm for assigning the density of newly fallen and wind-blown snow and provisional algorithms that realistically provide for snow erosion, accumulation, and packing by the wind.

Only *Lindsay*'s [1998] recent work has the temporal resolution that SNTHERM provides. Earlier studies of sea ice heat and mass budgets [e.g., *Semtner*, 1976; *Maykut and Untersteiner*, 1971; *Maykut*, 1978, 1982; *Hibler*, 1979; *Hibler and Ackley*, 1983; *Parkinson and Washington*, 1979; *Ebert and Curry*, 1993] have usually driven models with monthly averaged meteorological fields interpolated down to time steps of 1 day. Hibler and Hibler and Ackley, however, did use analyzed daily geostrophic fields as their forcing. The models by Semtner, Maykut, Hibler, Hibler and Ackley, and Parkinson and Washington are all for basin-scale climatological studies and thus have large horizontal grid spacing and coarse vertical grids. The Ebert and Curry model, in contrast, is one-dimensional with a finer vertical resolution and treats the physical processes in the snow and ice fairly completely. In particular, they include a detailed albedo parameterization that partitions the solar spectrum into four bands (most snow energy balance models use only two bands) and introduce a melt pond component that varies with time. *Lindsay* [1998] recently covered some of the same ground that we do. While we use one year of 3-hourly data from a single NP station to look in detail at processes in the air, snow, and ice, he uses 3-hourly data to define the climatological characteristics implied by 45 years of NP data. Although he and we consider the same heat budget terms in our respective models, his parameterizations are usually simpler to accommodate the vast quantity of data he is processing. For example, he uses constant coefficients with no stability dependence in his bulk parameterizations of the surface fluxes of latent and sensible heat. We, on the other hand, concentrate on developing state-of-the-art parameterizations for these turbulent fluxes. Because of these different emphases, our studies are complementary.

Maykut and Untersteiner's [1971] model, and many of the models described here that derive from it, uses a simple parameterization of the snow cover but still does a fairly good job of simulating the thermal regime and energy balance of the snow. *Ebert and Curry*'s [1993] model represents the next generation in the complexity of snow parameterization in sea ice models. SNTHERM, we feel, thus has a third-generation snow parameterization for sea ice models. In particular, SNTHERM models more in-snow processes than Ebert and Curry's model, has an order of magnitude more vertical resolution, and is forced with 3-hour data interpolated to hourly time steps, while their model uses monthly data interpolated to 8-hour time steps. Although a model of SNTHERM's complexity is not suitable for large-scale sea ice simulations, it is useful as a standard for assessing the assumptions of simpler models.

In addition to SNTHERM, several models have been developed in the past decade which contain detailed parameterizations of physical processes and energy and mass exchange within the snow cover [e.g., *Brun et al.*, 1989; *Bader and Weilenmann*, 1992; *Loth et al.*, 1993; *Gruell and Konzelmann*, 1994; *Lynch-Steiglitz*, 1994]. In particular, these models simulate snow cover properties such as density, grain size, and liquid water content over time. All of these properties are important in determining the optical properties and the thermal and hydrological processes in snow. In a study similar to ours, *Morris et al.* [1997] validate Bader and Weilenmann's model using in-snow temperature profiles from Halley Bay, Antarctica.

Here we use SNTHERM to model the processes at a single, drifting point on the surface near the North Pole with 3-hour NP-4 data. This provides a very detailed look at heat and mass

transfer not only at the surface but also within the snow cover. In fact, we validate our modeling by comparing its predicted in-snow and in-ice temperatures with NP-4 observations of these temperature profiles. In effect, by driving SNTHERM with the NP-4 3-hour data and by making reasonable assumptions about the values of variables not measured, such as snow density and salinity of the near-surface sea ice, we obtain an energetically consistent and temporally meaningful picture of the surface heat fluxes and, in so doing, validate SNTHERM as an important new tool for sea ice process studies.

2. Model Summary and Adaptations for North Pole 4

2.1. Numerical Model Overview

SNTHERM simulates most snow cover properties and processes, including heat conduction, phase change, water flow, snow ablation and accumulation, densification, grain growth, subsurface absorption of solar radiation, and surface energy exchange. The snow cover is modeled numerically as a one-dimensional, layered mixture of dry air, ice, liquid water, and water vapor. SNTHERM uses a control volume scheme [*Patankar*, 1980] with a moving mesh and a Crank-Nicholson scheme for the time domain. Control volumes coincide with the natural snow stratigraphy and are compressed over time as the snow compacts. Governing equations are linearized and solved with the Thomas algorithm; to obtain convergence, the time step adjusts automatically between 15 min for dry snow and 5 s during water flow.

SNTHERM models only thermal processes for soil layers and therefore includes a sink which artificially drains infiltrating water when it reaches the soil-snow interface. *Rowe et al.* [1995] simulated snowmelt on a Greenland ice sheet using a modified version of SNTHERM that replaces the underlying ground layer with ice. Their procedure makes advantageous use of the intralayer drain and avoids problems of ponding water, which are not handled in SNTHERM. We treat the sea ice layer in a similar fashion but additionally consider the effect of salinity on the thermal propoerties.

In this section we briefly describe the model, with particular emphasis on modifications for sea ice, for handling North Pole 4 data, and for computing turbulent exchange in stable stratification. *Jordan* [1991] and *Rowe et al.* [1995] give a more detailed description of SNTHERM. The current version of SNTHERM and a description of recent upgrades are available electronically from the corresponding author.

2.2. Energy and Mass Transfer Within the Snow and Sea Ice

One-dimensional mass balance equations for the total snow medium and the three water constituents (i = ice, ℓ = liquid water, v = water vapor) have the form

$$\frac{\partial}{\partial t}\int \rho_t\, dz = -\sum_{k=i,\ell,v}\sum_{S} \mathbf{J}_k\cdot\mathbf{n} \tag{1}$$

$$\frac{\partial}{\partial t}\int \gamma_k\, dz = -\sum_{S} \mathbf{J}_k\cdot\mathbf{n} + \sum_{k'=i,\ell,v}\int M_{k'k}(1-\delta_{k'k})\, dz. \tag{2}$$

Here t is time, ρ_t is the overall snow density, z is the vertical position relative to the interface between the snow and the sea ice, $\mathbf{J}_k$ is the flux of water constituent k (positive upward), and γ_k is the bulk density of that consituent. The integral is taken over a control volume of thickness Δz; and the summation Σ_S is over the top and bottom surfaces, where $\mathbf{n}$ is a unit vector normal to the surface. The source terms $M_{k'k}$ are the mass rates of melt, sublimation, and evaporation; $\delta_{kk'}$ is the Kronecker delta; $M_{kk'} = -M_{k'k}$; and discounting the gas component, $\rho_t \approx \gamma_\ell + \gamma_i$.

SNTHERM routes water through the snow with a simple gravitational formula [*Colbeck*, 1971], which computes the flux as

$$J_\ell = -\frac{K_\ell}{\mu_\ell}\rho_\ell^2 g = -\frac{K_{\max} s_e^\varepsilon}{\mu_\ell}\rho_\ell^2 g. \tag{3}$$

Here K_ℓ is the hydraulic permeability, ρ_ℓ is the density of water, g is the acceleration of gravity, μ_ℓ is the dynamic viscosity of water, $K_{\max}$ is the saturated permeability computed from *Shimizu*'s [1970] formula, and s_e is the effective saturation $(s - s_r)/(1 - s_r)$, where s is the liquid water saturation, s_r is the residual liquid water saturation (= 0.04), and the parameter ε is 3 [*Colbeck and Anderson*, 1982]. Because the model does not accommodate the ponding of water within the snow cover, we retain a finite permeability for ice crusts that may form from freezing meltwater.

After modifying SNTHERM for salinity, we adapted it to model thermal processes in either snow or sea ice. The one-dimensional equation for the conservation of energy is

$$\frac{\partial}{\partial t}\int \rho_t h_t\, dz = -\sum_{k=\ell,v}\sum_{S} h_k\mathbf{J}_k\cdot\mathbf{n} + \sum_{S} k_t\,\nabla\mathbf{T}\cdot\mathbf{n} + \sum_{S}\mathbf{R}_S\cdot\mathbf{n}, \tag{4}$$

where the subscript t refers to the total medium (snow or sea ice), T is temperature (in kelvins), k_t is the thermal conductivity, and R_S is net solar radiation (positive downward). The specific enthalpy h_k of a water constituent is

$$h_k = \int_{273.15}^{T} c_k(T)\, dT + L_k, \tag{5}$$

where c_k is the specific heat of the constituent at constant pressure, L_f and L_v are the latent heats of freezing and sublimation, and $h_t = \Sigma_{k=i,\ell,v} h_k$. The left-hand term in (4) represents the change in stored heat. Terms on the right represent heat fluxes due to water flow and vapor diffusion (disallowed for sea ice), conduction, and subsurface absorption of solar radiation.

The unfrozen bulk water density γ_ℓ and the gravimetric liquid water fraction f_ℓ are related to temperature depression (T_D = 273.15 K − T) through a formula developed by *Guryanov* [1985] for granular soil,

$$f_\ell(\text{snow}) \equiv \frac{\gamma_\ell}{\rho_t} = \frac{1}{1 + (a1T_D)^2}, \tag{6}$$

where we use $a1 = 1000\ \text{K}^{-1}$ for snow to approximate a step change in enthalpy around 0°C. For sea ice we modify *Maykut and Untersteiner*'s [1971] formula to a form commensurate with (6),

$$f_\ell(\text{sea ice}) = \frac{1}{1 + \dfrac{\rho_t T_D}{51.472\, S}} \qquad \text{for } S > 0.02 \text{ psu}, \tag{7}$$

where S is the salinity in practical salinity units (psu). Sensible and latent heat changes are combined in an apparent specific heat c_{app}, giving for the heat storage term in (4)

$$\left(c_t + L_\ell \frac{\partial f_\ell}{\partial T} + L_v \frac{\theta_v}{\rho_t} \frac{\partial \rho_{v,\text{sat}}}{\partial T}\right) \rho_t \Delta z \frac{\partial T}{\partial t} = c_{\text{app}} \rho_t \Delta z \frac{\partial T}{\partial t}, \quad (8)$$

where c_t is the specific heat of snow, θ_v is the fractional volume of water vapor, and $\rho_{v,\text{sat}}$ is the vapor density at saturation.

The thermal conductivity of snow is estimated from density ($\rho_s = \rho_t$) as

$$k_t = k_a + (7.75 \times 10^{-5} \rho_s + 1.105 \times 10^{-6} \rho_s^2)(k_t - k_a), \quad (9)$$

where k_a and k_t are the thermal conductivities of air and ice, and k_t varies with temperature as [*Glen*, 1974]

$$k_t = \frac{780}{T} - 0.615. \quad (10)$$

In (9) and (10), k_t, k_a, and k_t are in W m^{-1} K^{-1}, ρ_s is in kg m^{-3}, and T is in kelvins. Equation (9) fits *Yen*'s [1962] data and extrapolates to the conductivity of ice. The presence of brine reduces the conductivity of ice by [*Untersteiner*, 1961]

$$k_{si} = k_t - \frac{BS}{T_D} \qquad T_D \geq 0.05411\ S, \quad (11)$$

where $B = 0.13$ W m^{-1}. SNTHERM includes the diffusion and condensation of water vapor when it computes effective thermal conductivity, but the effect is only significant for low density, warm snow.

The solar absorption term in (4) depends on the intensity, angle, and spectral composition of the incident radiation and on snow albedo, optical depth, and grain diameter. SNTHERM splits the incident solar radiation into high-energy and low-energy spectral bands with wavelength ranges of 0.4–1.12 μm and 1.12–2.4 μm, respectively. Radiation in the low-energy band is totally absorbed within the model's top node. Radiation in the high-energy band decays within the snow according to Beer's law with an asymptotic bulk extinction coefficient of [*Bohren and Barkstrom*, 1974; *Anderson*, 1976]

$$\beta_\infty = \frac{0.003795 \rho_t}{\sqrt{d}}. \quad (12)$$

Here β_∞ is in m^{-1} when ρ_t is in kg m^{-3} and the grain size d is in meters.

Equation (12) is inappropriate for higher-density snow, however, because this functional relationship assumes discrete scatterers. For a porosity less than 0.38 (generally that of random packing) we use a linear interpolation between (12) and the extinction coefficient 1.5 m^{-1} of white ice under cloudy skies [*Grenfell and Maykut*, 1977]. Coefficients in wet snow are about half those in cold, dry snow [*Perovich*, 1996]; we accordingly decrease (12) linearly with liquid water saturation up to a maximum of one half when the saturation is 15%. The fraction of net solar radiation in the 0.4–1.12 μm spectral band, f_{high}, increases with cloud fraction N as

$$f_{\text{high}} = f_{\text{high0}}(1 - N) + (f_{\text{high0}} + 0.17)N, \quad (13)$$

where f_{high0} (= 0.41) is the fraction under clear skies. For sea ice we also use an extinction coefficient of 1.5 m^{-1} [*Maykut and Untersteiner*, 1971].

2.3. Snow Cover Accumulation and Metamorphism

SNTHERM accumulates snow in specified nodal increments (of 2 cm) using either the measured or the estimated density for the new snow. In our case, density was unavailable; we thus estimated it using a function developed for NP-4. New-snow density shows a general increase with air temperature [*LaChapelle*, 1961; *Meister*, 1985; *McGurk et al.*, 1988] and wind speed [*Kotlyakov*, 1961]. Other factors, such as grain size and crystal type, also affect the density, but they have not been parameterized. In general, smaller crystals with simpler shapes pack most efficiently and lead to denser snow covers. Correspondingly, *Meister* [1985] observes that new-snow density increases when air temperature is below −15°C, presumably because crystal type changes from dendritic to columnar and disk-shaped forms [*Magono and Lee*, 1966; *Colbeck et al.*, 1990]. Because high-Arctic snow is fragmented by wind and often crystalizes at very low temperatures, it is fine grained and tends to have a higher density than snow at warmer, more sheltered locations.

Our function for new-snow density combines *Meister*'s [1985] temperature parameterization with the wind dependence observed by *Kotlyakov* [1961]. Meister's data, as well as those of *LaChapelle* [1961] and *McGurk et al.* [1988], do not show a significant effect of wind speed on new-snow density, in part because their measurements came from sites sheltered from high winds. In the temperature range from −5° to −10°C and for 10-m winds between 6 and 30 m s^{-1}, Kotlyakov reports a parabolic dependence of new-snow density on wind speed; while at speeds less than 6 m s^{-1}, he observes densities close to zero.

We incorporated wind and temperature effects in an exponential function that limits the maximum new-snow density, ρ_{ns}, to 500 kg m^{-3}:

$$\rho_{\text{ns}} = 500[1 - 0.951 \exp(-1.4(278.15 - T_a)^{-1.15} - 0.008 U_{10}^{1.7})] \quad (14a)$$

for $260.15 < T_a \leq 275.65$ K

$$\rho_{\text{ns}} = 500[1 - 0.904 \exp(-0.008 U_{10}^{1.7})] \quad (14b)$$

for $T_a \leq 260.15$ K.

In these, T_a is the air temperature at 2 m in kelvins and U_{10} is the 10-m wind speed in m s^{-1}. Because of uncertainty in *Meister*'s [1985] function at lower temperatures, in the range where simpler crystal types predominate, we write (14b) with no dependence on temperature for temperatures below −13°C.

Figure 2 shows the wind dependence of ρ_{ns} predicted by (14) for 2-m air temperatures of −13°, −3°, and 2°C; the measurements of *Kotlyakov* [1961]; and the temperature parameterization of *Meister* [1985]. In representing Meister's function we assumed a wind speed of 3 m s^{-1}. For winds between 6 and 15 m s^{-1}, (14) predicts an increase in density of about 20 kg m^{-3} for each m s^{-1} of wind speed. *Bilello*'s [1984] analysis of seasonal snow density data in the former USSR and the generalized observations of *Bogorodskii* [1975] corroborate this rate of increase. Figure 2, as well as the other cited data sets, shows considerable scatter, with standard errors of the order of 40–50 kg m^{-3}. Combining temperature and wind effects (as in (14)) should reduce the error, but in all likelihood significant scatter remains.

Blowing and drifting snow and the topography of the under-

lying sea ice caused considerable spatial variability in snow depth at NP-4. *Buzuev and Dubovtsev* [1978] and *Buzuev et al.* [1979] describe and analyze this variability in more detail. To simulate this variability in snow depth, we added a horizontal transport or advection function to SNTHERM which erodes or accumulates snow when it is redistributed by wind. We could have developed a time series of advected snow data to drive this function, selected to fit observed snow depth, but instead propose a physically based formula related to wind speed and surface snow conditions. The total wind transport G (in kg m^{-1} s^{-1}) of snow within 0.5 m of the surface is approximated by [*Schmidt*, 1986; *Tabler et al.*, 1990]

$$G = (a2/\rho_a^{1/2}g)(\tau^{1/2} - \tau_t^{1/2})(\tau - \tau_t), \qquad (15)$$

where ρ_a is air density, τ is the surface stress, and τ_t is the surface stress at which snow begins to drift. The parameter $a2$ depends on wind and snow conditions. It is generally lower for fresh, dry snow and declines logarithmically with roughness length z_0 [*Schmidt*, 1986]. We assumed a relatevely low value of $a2 = 5$, appropriate for winter snow at NP-4 and consistent with our 1-mm selection for z_0.

Although most other workers in this field formulate (15) in terms of the friction velocity u_*, we prefer to use the surface stress τ. In rigorous usage, u_* does not depend on horizontal or vertical position in the atmospheric surface layer, while τ is not bound by such constraints. In fact, the horizontal and vertical variations in τ over a surface that is not horizontally homogeneous is what causes one area to be scoured of snow and another to form drifts.

By invoking conservation of mass, we compute from (15) the snow erosion or deposition rate J_{bl} (henceforth referred to as the advection flux) as the gradient of G in the direction x of the wind vector [*Pomeroy et al.*, 1993]. Differentiating (15) gives

$$J_{bl} = (a2/\rho_a^{1/2}g)\left(\frac{1\partial\tau}{\tau\partial x}\right)(\tfrac{3}{2}\tau^{3/2} - \tau\tau_t^{1/2} - \tfrac{1}{2}\tau^{1/2}\tau_t). \qquad (16)$$

We "tune" the fractional stress gradient, $\tau^{-1}\partial\tau/\partial x$, to adjust the advection flux to match observed snow depth variations at NP-4. A positive gradient removes snow; a negative gradient deposits it. The fractional stress gradient is site specific. We also expect it to vary temporally with changing snow conditions, but as we discuss in section 4.2, $\tau^{-1}\partial\tau/\partial x$ required, at most, one-annual adjustments to reproduce observed snow depths at NP-4.

The threshold friction velocity ($u_{*t} = (\tau_t/\rho_a)^{1/2}$) typically ranges from 0.15 to 0.25 m s^{-1} for loose, dry, unbonded snow and from 0.25 to 1.00 m s^{-1} for older, wind-hardened, dense or wet snow [*Li and Pomeroy*, 1997], although values as low as 0.07 m s^{-1} are reported for exceptionally light snow [*Kind*, 1981]. Surface resistance to erosion depends on snow density, grain size, bond area, and snow wetness. The threshold velocity is also dynamically affected by the impact of airborne snow particles on the snow surface. *Schmidt* [1980], in fact, shows that the wind velocity required to dislodge even slightly bonded snow through fluid drag alone is unrealistically high; thus it is also necessary to consider the impact force of airborne snow. Because there is no satisfactory procedure for estimating the threshold velocity, *Schmidt* [1986] stresses the need for direct measurement of this parameter.

While acknowledging the limitations of a simple parameterization, we represented the general trends in u_{*t} at NP-4 with a function related to snow cohesion:

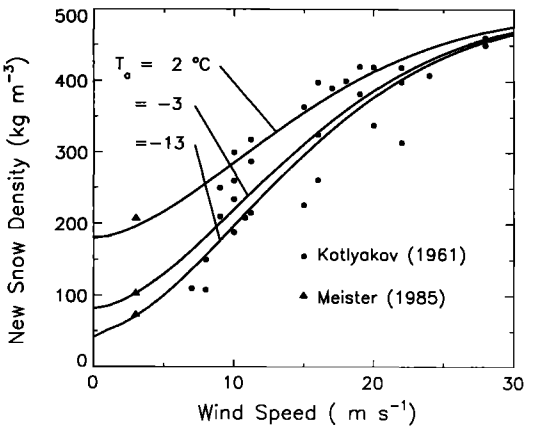

Figure 2. New-snow densities predicted by (14) for a range of 10-m wind speeds and 2-m air temperatures (solid lines). The dots are data from *Kotlyakov* [1961], measured in a temperature range between −10° and −5°C, and the triangles are *Meister*'s [1985] temperature relationship at an assumed wind speed of 3 m s^{-1}.

$$u_{*t} = a3 + c3[(1 - \phi)n1(d_b/d)^2]^{b3}. \qquad (17)$$

The quantity in brackets is proportional to cohesive strength per unit area, where ϕ is the snow porosity, $n1$ is the coordination number (number of contacts per grain), and d_b is the bond diameter. We estimated $n1$ with a polynomial, $n1 = 12.91 - 24.52\phi + 11.88\,\phi^2$, which fits *Keeler*'s [1965, Table 2] data. We set $a3 = 0.2$ as a minimum value for u_{*t}, assumed that $b3$ is 0.5, and selected $c3$ as 4.0, so that $u_{*t} = 1.0$ m s^{-1} for wind-hardened snow (for $\phi = 0.6$, $n1 = 2.5$, and $d_b/d = 0.20$). We included a multiplicative factor of 1.29 for increased cohesion in wet snow [*Li and Pomeroy*, 1997]. Our intent with the parameterization scheme in (16) and (17) is not to propose a universal procedure for wind redistribution of snow, since we do not have data to support this. Rather (16) and (17) provide a reasonably realistic and systematic way to build the snow cover for this simulation.

The modeled deformation rate accounts for the settling of new snow caused by destructive metamorphism, compaction under the sustained pressure of the snow overburden, loss of snow structure during active melting, and wind packing:

$$\frac{\partial}{\partial z}\frac{\partial z}{\partial t} = \left[\frac{\partial}{\partial z}\frac{\partial z}{\partial t}\right]_{\text{metamorphism}} + \left[\frac{\partial}{\partial z}\frac{\partial z}{\partial t}\right]_{\text{overburden}} + \left[\frac{\partial}{\partial z}\frac{\partial z}{\partial t}\right]_{\text{melt}} + \left[\frac{\partial}{\partial z}\frac{\partial z}{\partial t}\right]_{\text{wind}}. \qquad (18)$$

In our numerical implementation, the position vector z coincides with the control volume node, which moves with the compacting snow cover.

As the result of studies in Hanover, New Hampshire, during the winters 1994 through 1996, we revised the SNTHERM compaction routine published by *Jordan* [1991]. These revisions include decreasing the density cutoff for the initial metamorphic phase of 1% per hour from *Anderson*'s [1976] suggested value of 150 kg m^{-3} to the lesser of 15% above the new snow density or 100 kg m^{-3}, decreasing snow viscosity from 3.6×10^6 to 1.0×10^6 kg s m^{-2}, and reducing the enhancement factor for the presence of water from 2.0 to 1.5. As before, reducing the control volume thickness to maintain a constant

density compensates for mass losses in nodes undergoing melting.

For NP-4 we added a provisional wind-packing term per unit area which increases with wind transport G and decreases exponentially with the overburden $\rho_s g z'$, where z' is the depth below the snow surface:

$$\left[\frac{\partial}{\partial z}\frac{\partial z}{\partial t}\right]_{\text{wind}} = a4b4G \exp^{-c4(T-273\,15)-d4\,\rho_s g z'} \quad \text{for } u* \geq u_t*, \tag{19a}$$

where

$$b4 = 1 \qquad \text{for } \rho_s < 400 \text{ kg m}^{-3}$$

$$b4 = e^{-e4(\rho_s - f4)} \qquad \text{for } \rho_s \geq 400 \text{ kg m}^{-3}. \tag{19b}$$

We arbitrarily let the wind factor decay to one half for an overburden of 7.9 N m^{-2} (e.g., when $z' = 0.01$ m and $\rho_s = 80$ kg m^{-3}); therefore $d4 = 0.0884$ m^2 N^{-1}. We also set the surface compaction rate at 10% per hour when U_8 is 8 m s^{-1}, the threshold wind speed U_{8t} is 4 m s^{-1}, and T is 0°C; thus $a4 = 2.66 \times 10^{-3}$ s^{-1}. Except for the higher-density threshold, $f4 = 400$ kg m^{-3}, the temperature and density dependencies in (19) resemble *Anderson*'s [1976] metamorphic term. We thus arbitrarily use the same fitting parameters: $c4 = 0.04$ K^{-1} and $e4 = 0.046$ m^3 kg^{-1}. In addition to compaction, SNTHERM computes density changes due to ice sublimation and refreezing meltwater.

SNTHERM computes grain growth for dry snow as a function of vapor flux [*Jordan*, 1991] based on a formula used to predict growth by sintering in metals and ceramics [*Stephenson*, 1967; *Gow*, 1969],

$$d^2 = d_0^2 + a5 \min(|J_v|, 1 \times 10^{-6})t, \tag{20}$$

where d_0 is the initial snow diameter, $a5 = 1 \times 10^{-6}$ m^4 kg^{-1}, J_v is the mass vapor flux, and t is time in seconds. In wet snow, where there is a marked increase in grain growth [*Colbeck*, 1982], SNTHERM relates grain growth to liquid water content. In both cases, growth is inversely related to grain size, and 5 mm is the maximum size permitted.

For NP-4 we added a provisional bond growth equation to estimate snow strength for equation (17). *Hobbs and Mason* [1964] apply classical sintering theory to compute bond growth between ice spheres in the laboratory,

$$\frac{d_b}{d} = \frac{a6(T)t^r}{d^p}, \tag{21}$$

where r is 0.2, $a6(T)$ is a temperature dependent coefficient that varies with the sintering mechanism, and p is 0.6. For this study, we retained p as 0.6 but selected r as 0.67 to match the higher bond growth rates observed by *Keeler* [1965] in a dry, natural snow cover. We also selected $a6$ ($= 8.75 \times 10^{-8}$ m$^{0\,6}$ s$^{-0.67}$) to fit the data of Keeler and included the exponential increase in cohesion with temperature measured by *Hosler et al.* [1957]. As with grain growth, we related bond growth in wet snow to liquid water content and to inverse grain size. SNTHERM sets upper limits on the bond-to-grain size ratio of 0.30 and 0.40, respectively, for dry and wet snow.

2.4. Surface Exchange With the Atmosphere

The meteorologically determined fluxes of mass and energy prescribe the upper boundary conditions at the snow surface. The energy flux F above the surface is

$$F = R_S + R_L - F_{\text{sens}} - F_{\text{lat}} - F_{\text{prec}}, \tag{22}$$

where R_S is the net solar radiation, R_L is the net longwave radiation, F_{sens} and F_{lat} are the turbulent fluxes of sensible and latent heat, and F_{prec} is heat convected by precipitation. In our convention, positive F warms the surface, as does positive R_S and R_L, and negative F_{sens}, F_{lat}, and F_{prec}.

Emitted longwave radiation is usually computed from the Stefan-Boltzmann equation with the incoming component either measured or estimated. Because only periodic, manual samples of net longwave radiation were available at NP-4, we computed net longwave radiation as the residual of total and net solar radiation. We made alternative runs using these data and R_L computed from *Makshtas et al.* [1998]

$$R_L = \varepsilon\sigma(\varepsilon_* T_a^4 - T_0^4), \tag{23}$$

where the snow emissivity ε is 0.99, T_0 is surface temperature, σ is the Stefan-Boltzmann constant, and the sky emissivity ε_* is expressed in terms of cloud cover as $0.765 + 0.22N^3$ [*König-Langlo and Augstein*, 1994].

The turbulent fluxes are computed from [*Andreas*, 1996]

$$F_{\text{sens}} = [\rho_a c_p C_{Hr} U_r + E_0](T_0 - T_r) \tag{24}$$

$$F_{\text{lat}} = C_{Er}\rho_a L_v U_r(Q_0 - Q_r). \tag{25}$$

Here c_p is the specific heat of air at constant pressure; C_{Hr} and C_{Er} are the bulk transfer coefficients for sensible and latent heat appropriate at reference height r above the snow or sea ice surface; U_r, T_r, and Q_r are the wind speed, air temperature, and specific humidity at a height r; and T_0 and Q_0 are the same quantities at the surface. E_0 is a windless transfer coefficient that we feel improves sensible heat predictions when the atmosphere is stably stratified. We found no significant effect, however, of including a windless coefficient for latent heat.

The bulk transfer coefficients are computed from the roughness lengths z_0, z_T, and z_Q for momentum, heat, and moisture as

$$C_{Hr} = \kappa^2\left[\ln(r/z_0) - \psi_m\left(\frac{r}{L}\right)\right]^{-1}\left[\ln(r/z_T) - \psi_h\left(\frac{r}{L}\right)\right]^{-1}, \tag{26}$$

$$C_{Er} = \kappa^2\left[\ln(r/z_0) - \psi_m\left(\frac{r}{L}\right)\right]^{-1}\left[\ln(r/z_Q) - \psi_h\left(\frac{r}{L}\right)\right]^{-1}, \tag{27}$$

where κ ($= 0.4$) is the von Kármán constant, ψ_m and ψ_h are the integrated forms of the profile corrections for diabatic conditions, and L is the Obukhov length [*Launiainen and Vihma*, 1990],

$$L = -\frac{\rho_a u_*^3}{\kappa g\left(\dfrac{F_{\text{sens}}}{\bar{T}c_p} + 0.61\dfrac{F_{\text{lat}}}{L_v}\right)}. \tag{28}$$

Here $\bar{T}$ is a representative temperature (in kelvins) of the surface layer, and the friction velocity u_* is

$$u_* = \kappa U_r[\ln(r/z_0) - \psi_m(r/L)]^{-1}. \tag{29}$$

Although there is some evidence that z_0 increases with wind speed over snow-covered surfaces [e.g., *König*, 1985], we do not see that behavior in our recent work over sea ice [*Andreas and Claffey*, 1995]. Consequently, we take z_0 to be constant and set it to 1 mm, a typical value for sea ice [*Banke et al.*, 1980; *Overland*, 1985; *Andreas and Claffey*, 1995].

In most energy balance simulations, z_0, z_T, and z_Q, the three roughness lengths are taken as equal. Experimental and theoretical evidence shows, however, that z_T/z_0 and z_Q/z_0 decrease with increasing wind speed; we estimate z_T and z_Q from the roughness Reynolds number using the method described by *Andreas* [1987a].

For unstable stratification ($r/L < 0$), the ψ functions are [e.g., *Paulson*, 1970]

$$\psi_m = \ln\left(\frac{1+x^2}{2}\right) + 2\ln\left(\frac{1+x}{2}\right) - 2\arctan x + \frac{\pi}{2} \quad (30)$$

$$\psi_h = 2\ln\left(\frac{1+x^2}{2}\right), \quad (31)$$

where

$$x = \left(1 - 16\frac{r}{L}\right)^{1/4}.$$

Numerous ψ functions have been proposed for the stably stratified atmosphere ($r/L > 0$) [*Andreas*, 1996; *Carson and Richards*, 1978]. In the neutral to slightly stable regimes ($r/L < 0.5$), general consensus supports a log-linear form:

$$\psi_m = \psi_h = -b\frac{r}{L}, \quad (32)$$

where b ranges from 5 to 7. Most snow models extend the log-linear relationship into the very stable regime as well, although (32) has been tested only out to $r/L = 1$, and considerable evidence suggests that the turbulent structure changes for r/L above 0.5–1.0. *Andreas* [1996] suggests using the more recent function of *Holtslag and de Bruin* [1988] and *Beljaars and Holtslag* [1991], which he refers to as the Dutch formulation. In this formulation, the authors fitted a continuous function to three piecewise regimes [*Hicks*, 1976; *Carson and Richards*, 1978] giving

$$\psi_m = \psi_h = -\left[\frac{0.70r}{L} + 0.75\left(\frac{r}{L} - 14.3\right)\cdot\exp\left(\frac{-0.35r}{L}\right) + 10.7\right]. \quad (33)$$

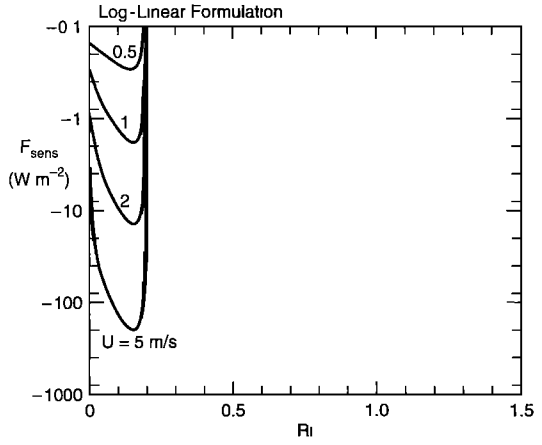

Figure 3. Sensible heat flux computed with (24) (with $E_0 = 0$) and the log-linear stability correction (with $b = 5$) for a 2-m air temperature of −10°C and for several values of the 2-m wind speed. The abscissa is the gradient Richardson number, $Ri = (g/\bar{T})\,([\partial T_r/\partial z + 0.61\bar{T}\partial Q_r/\partial z]/(\partial U_r/\partial z)^2)$.

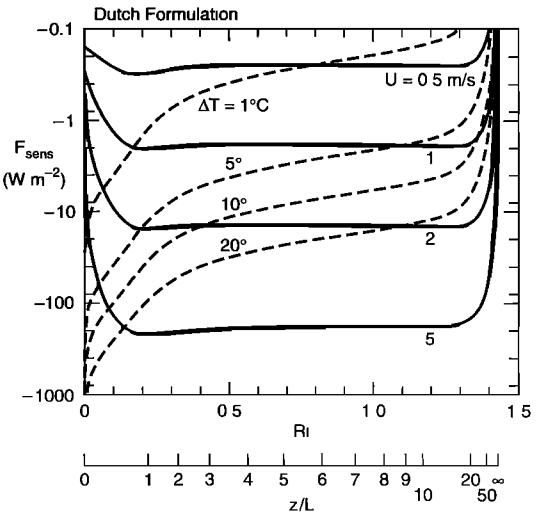

Figure 4. As in Figure 3 except this uses the Dutch stability correction. The solid lines show the fluxes for various 2-m wind speeds; the dashed lines, for various air-surface temperature differences.

For small r/L, (33) approaches the log-linear form with $b = 5.2$.

An analysis used by *Carson and Richards* [1978] and *Halberstam and Melendez* [1979] demonstrates the comparative effects of the log-linear and Dutch formulations on the turbulent heat fluxes. We do a similar analysis and thus show in Figures 3 and 4 the sensible heat flux as a function of stability (r/L and the gradient Richardson number Ri) for 2-m wind speeds of 0.5, 1, 2, and 5 m s^{-1} for the two formulations. To generate the curves, we hold the 2-m air temperature constant at −10°C and increase stability by lowering the surface temperature. As the snow surface cools below the air temperature, the surface initially extracts more heat from the air. With increasing stability, however, buoyant forces strongly damp the turbulent exchange until mechanical production can no longer maintain it. Consequently, as stability continues to increase, F_{sens} falls rapidly to zero. For the log-linear formulation, buoyancy damping decouples the snow surface from the atmosphere at a critical Richardson number of $Ri_{cr} = 0.20$ (Figure 3). For the Dutch formulation, however, the turbulent range is considerably longer (Figure 4). Here Ri_{cr} is 1.43. Although Ri_{cr} is traditionally assumed to be 0.20–0.25 [e.g., *Okamoto and Webb*, 1970], *Andreas* [1996] reviews atmospheric observations that suggest Ri_{cr} can be as high as the Dutch formulation limit of 1.43.

By observing where the ΔT isotherms cross the 1-m s^{-1} wind speed curve in Figure 4, we see that sensible heat exchange ceases at a temperature difference of 1°C for the log-linear formulation (where $Ri_{cr} = 0.2$) but continues beyond 5°C for the Dutch formulation. For wind speeds much below 1 m s^{-1}, it is virtually certain that the snow surface will decouple from the atmosphere. That is, Figure 4 shows that such low winds are unable to sustain much sensible heat exchange, and even a small temperature difference will totally suppress the turbulence.

King and Connolley [1997] also discuss this problem of estimating the sensible heat transfer in stable stratification. Their emphasis is on flux calculations in global climate models (GCMs); they identify two problems. First, many GCMs, which

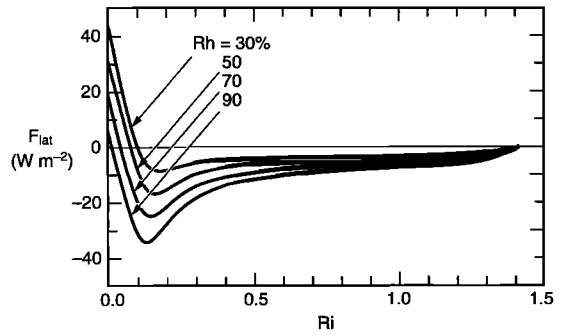

Figure 5. Latent heat flux computed with (25) using the Dutch form for the stability correction for several values of relative humidity, a 2-m air temperature of −10°C, and a 2-m wind speed of 5 m s^{-1}. The abscissa is the gradient Richardson number.

use some form of the *Louis* [1979] heat flux parameterization, overestimate the magnitude of the sensible heat flux in stable conditions. Second, as we have shown, in light winds, when the log-linear stability corrections become large and negative and thereby reduce the transfer coefficients to zero, there is no mathematical way to sustain a sensible heat flux. King and Connolley treat both of these issues by using the log-linear stability functions, (32), but by limiting the gradient forms of both ψ_m and ψ_h (i.e., ϕ_m and ϕ_h) to values of −11 or larger. Even with this solution though, the turbulent fluxes go to zero as the mean wind speed goes to zero. Thus there is still no way to prevent extraordinary surface cooling in response to radiative losses.

For such low-wind conditions we therefore propose adding a windless coefficient E_0 in (24). To our knowledge, no one has attempted such a bulk parameterization in stable stratification; but *Godfrey and Beljaars* [1991] and *Fairall et al.* [1996] recognize that in unstable stratification, coherent structures still foster significant heat exchange though the mean wind speed might be near zero. We hypothesize that in stable stratification, E_0 arises because of the gustiness caused by breaking internal gravity waves, which are common in stable boundary layers [*Rees*, 1994]. Although we hope eventually to parameterize E_0 in terms of boundary layer variables, for now we take E_0 as constant. Empirical evidence suggests its value is around 0.5 to 1 W m^{-2} K^{-1}.

As a complement to Figures 3 and 4, Figure 5 shows how stability influences the latent heat flux for air of various relative humidities (computed with respect to ice). For stable stratification the latent heat flux is always positive (sublimation) at neutral stability for relative humidities less than 100%. The flux decreases in magnitude, however, with increasing stability and, depending on the relative humidity, eventually changes direction when the surface cools below the dew point. As Ri approaches 1.43, turbulence ceases, and the latent heat flux goes to zero, as the sensible heat flux did. These low-wind, high-humidity conditions are just those that lead to surface hoar and riming overnight.

Figures 4 and 5 explain the heat flux regimes commonly observed over snow-covered surfaces. The three most common modes are $F_{sens} > 0$, $F_{lat} > 0$; $F_{sens} < 0$, $F_{lat} > 0$; and $F_{sens} < 0$, $F_{lat} < 0$ [*Andreas*, 1987b; *King and Anderson*, 1994; *Andreas and Cash*, 1996]; the two latter are the dominant modes in stable stratification. We see from Figure 5 that stability dictates which of these two transfer modes obtains in a stable boundary layer. Near-neutral stratification favors the $F_{sens} < 0$, $F_{lat} > 0$ mode; increasing stability favors the $F_{sens} < 0$, $F_{lat} < 0$ mode.

Except for the new wind redistribution material, the parameters discussed above are standard SNTHERM default values and have not been tuned to the NP-4 site. While most of these are fixed within the code, some may be varied by the user. Table 1 summarizes SNTHERM input parameters for our baseline simulations. Later in the paper, we use alternative turbulent transfer schemes and examine how they effect snow temperature predictions.

3. Data From North Pole 4

3.1. Site and Available Data

Under the leadership of D. L. Laikhtman, NP-4 was the first Russian drifting station to concentrate on measuring the surface heat budget in the summer (August–September 1956). *Kucherov and Sternzat* [1959] describe the NP-4 meteorological site, the instruments used during these summer measurements, sampling procedures, and some data reduction methods. Some of these instruments were also used before and after this special summer experiment for a 1-year investigation (April 1956 to April 1957) of the components of the heat budget over different parts of the multiyear sea ice floe on which NP-4 was located. *Nazintsev* [1964] describes some of these year-long observations. The data set available from NP-4 includes standard meteorological observations (also described on the *NSIDC* [1996] CD-ROM), standard radiation observations [*Marshunova and Mishin*, 1994], atmospheric surface layer temperature and wind speed profile measurements, and numerous temperature profile measurements in snow, in sea ice of different ages, and in melt ponds.

Nazintsev [1963, 1964] presents some of these data in generalized form, but some have never been used in any analyses. We reconstructed these data from the original records archived at AARI. Of course, using historical data brings up questions about their accuracy and requires, at least, a short description of the methods and instruments used to obtain them. Although none of us has any first-hand experience with the sampling on NP-4, the station personnel seemed to be careful and conscientious. For example, Nazintsev himself conducted most the meteorological measurements in collaboration with another well-known polar scientist, I. G. Petrov.

Table 1. Parameters Used in the Baseline SNTHERM Simulation

Parameter	Value
Roughness length for momentum (z_0)	1 mm
Roughness lengths for heat (z_T) and moisture (z_Q)	computed from *Andreas* [1987a]
Stability correction for stable stratification	Dutch formulation, equation (33)
Windless exchange coefficient for sensible heat (E_0)	1.0 W m^{-2} K^{-1}
Snow emissivity (ε)	0.99
Fraction of incoming solar radiation with wavelengths <1.12 μm (f_{high})	0.41
Irreducible liquid water saturation (s_r)	0.04
Snow viscosity	1.0 × 10^6 kg s m^{-2}
Density cutoff for metamorphic compaction	min (100 kg m^{-3}, 1.15ρ_{ns})

Kucherov and Sternzat [1959] describe the preexperiment calibrations performed, especially on the temperature sensors, and the real-time quality control done on NP-4. *Radionov et al.* [1996] also describe in detail many of the measurements and the quality controls on the North Pole drifting stations, though particularly emphasizing the snow measurements.

One of us (A.P.M.) was deeply involved in overseeing the conversion of the hard copy NP-4 meteorological data from the AARI archives into the electronic files that we used in this study and which went into the *NSIDC* [1996] CD-ROM. During this process, AARI personnel again continually monitored the quality and consistency of the data.

For this paper, we prepared from the *NSIDC* [1996] CD-ROM and the AARI archives a special data set that included (1) standard meteorological and radiation data, (2) data from a vertical array of copper resistance-wire thermometers (CWTs) installed in and above 2-year ice (henceforth referred to as location A), and (3) a vertical array of thermocouples in the snow above multiyear ice (called location B).

Briefly, to drive SNTHERM, we used standard meteorological data.

1. Wind speed at 8 m was measured with a light board (measurement error about ± 1 m s^{-1}) mounted on a wind vane. The light board is a type of pendulum anemometer [*Middleton and Spilhaus*, 1957, p. 151].
2. Air temperature and humidity was measured at a height of 2 m. For air temperatures above -30°C, these were measured in a radiation screen with dry-bulb and wet-bulb mercury thermometers (with a temperature error of not more than ± 0.2°C and with an error in relative humidity of about 10% when the air temperature was above -10°C). Below -30°C, temperature was measured with an alcohol thermometer (error about ± 0.8°C). The humidity sensors, however, did not function well below -10°C, and for the winter we used monthly climatological humidity data from *Vowinckel and Orvig* [1970].
3. Surface-layer pressure was computed from 3-hourly measurements made with a mercury barometer having a maximum error of ± 0.5 mbar.
4. Precipitation at a height of 2 m was measured with a shielded Tretyakov gauge.

All of these measurements, except for precipitation, were manual samples taken every 3 hours. For the modeling, we interpolated linearly between data points to obtain hourly values. Precipitation was reported twice daily at noon and midnight. We corrected the gauge readings with the procedure described in section 4.2.

From the available radiation data, which include direct solar radiation, diffuse radiation, global radiation, reflected radiation, and net radiation, we used only hourly averaged values of global radiation (the only quantity recorded on paper tape) and albedo, which we computed from the periodic, manual samples of global and reflected solar radiation. Using these albedo values, we estimated averaged reflected solar radiation from the hourly global radiation data. In principle, it is possible to use as an external parameter of the model the longwave radiation balance, calculated as the difference between the measured net radiation and the global and reflected radiation. However, as *Marshunova and Mishin* [1994] explain, the longwave radiation and radiation balance data measured with balance meters have significant systematic errors of up to 30%. So we use these data only for checking the consistency of model results and for calculating the longwave radiation balance. In our opinion the accuracy of the radiation is not better than the reporting increment in which the data were originally tabulated, 0.01 MJ m^{-2} h^{-1} for the hourly global radiation and 0.01 cal cm^{-2} min^{-1} for the manual samples, which are ~3 and 7 W m^{-2}. We compute a combined error in net solar radiation of around 10 to 13 W m^{-2} during maximum insolation in June.

To initialize the model and to validate its results, we used the in-snow and in-ice temperature profiles measured with the thermometers mentioned above. At location A there was an array of CWTs, each with a resistance of 235 Ω at 0°C. The Main Geophysical Observatory in Leningrad produced these thermometers. Depending on weather conditions, they were monitored 1 to 4 times per day with a Wheatstone bridge. *Kucherov and Sternzat* [1959] investigate the accuracy of these measurements and find it to be about ± 0.1°C. At location B the snow temperature profiles were measured with copper-constantan thermocouples monitored with a galvanometer. These measurements probably have an accuracy no better than ± 0.2°C. During the summer, measured temperatures in the upper 5 to 10 cm of the snowpack can be several degrees too high because of solar heating of the sensors.

3.2. Meteorological Conditions at North Pole 4 (1956–1957)

The drift track of NP-4 between April 30, 1956 and April 4, 1957, was very near the North Pole and provides us an opportunity for investigating the meteorological conditions at this most northly of polar regions. Figure 6 shows the available meteorological data for the year. The figure also shows surface temperature, measured with an alcohol thermometer.

The winds during the NP-4 drift were strong, typically 4–7 m s^{-1} and frequently exceeding 10 m s^{-1}. The 2-m air temperature ranged from $+1.5$°C in summer to -45°C in mid-January 1957. During the summer melt period the air temperature remained near 0°C. We suspect that the low clouds were in radiative equilibrium with the melting snow. The presence of a deep, persistent cloud cover over the region is also evidenced by high humidity and small fluctuations in the surface pressure during this time. Air temperature dropped rapidly after September 18, 1956 (day 262), around the start of polar night. In contrast to the summer, during late fall and winter, temperature swings associated with the passing of synoptic systems were up to ± 40°C.

The hourly solar signal clearly shows diurnal fluctuations; the 3-hour series of air and surface temperatures during the transition months of May, June, and September also show a diurnal signal. From 1 year of data from the Arctic Ice Dynamics Joint Experiment (AIDJEX) at lower latitudes in the Beaufort Sea, *Baumann* [1978] also found diurnal air temperature variations only in spring and fall. Daily temperature maxima were usually at 1800 UTC. Albedo was high in the spring (0.80–0.90), consistent with a surface covered with small-grained, dry snow. Typically, the presence of melt ponds and exposed sea ice in the summer leads to lower surface albedos. Because snow cover remained over most of the NP-4 site during the summer, including the radiometer location, the minimum measured albedo of around 0.6 is higher than expected for summer sea ice [*Nazintsev*, 1964].

4. Model Simulations

4.1. Model Initialization

We ran two SNTHERM simulations: between May 30, 1956 and April 4, 1957, at location A, collocated with the CWT

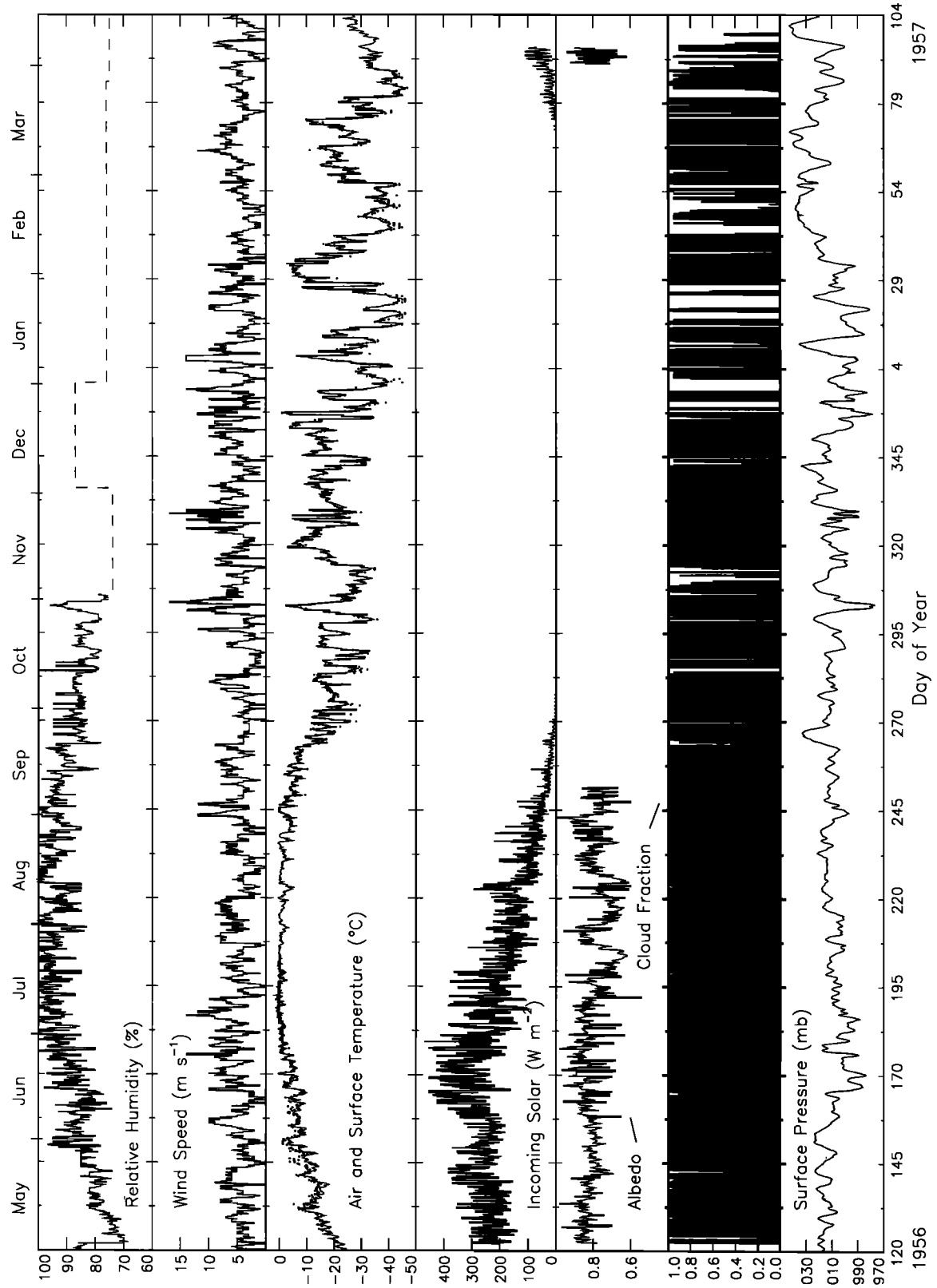

Figure 6. Relative humidity, wind speed, air temperature, incoming solar radiation, albedo, cloud fraction, and surface pressure on NP-4 between April 30, 1956 and April 4, 1957. Solar radiation and albedo are hourly and 6-hourly series, respectively; other series are 3 hourly. The temperature plot also shows the measured surface temperature as dots. The dashed lines are average monthly relative humidity from *Vowinckel and Orvig* [1970].

Table 2. Snow Density With Depth for Different Snow Types [*Radionov et al.*, 1996]

Depth cm	Fresh, Dry kg m^{-3}	Fresh, Moist kg m^{-3}	Old, Compact kg m^{-3}	Wet and Melting kg m^{-3}	Firn kg m^{-3}	Ice Crust kg m^{-3}
0–5	150	230	280	480		
6–10	190	260	330	530		
11–30	240	290	350	530		
31–40			360			860
41–70			380		630	
>70			440			

arrays in and above 2-year ice; and between April 30 and December 31, 1956, at location B, collocated with the thermocouple array on multiyear ice. In both cases we subdivided the snow and sea ice layers into control volumes having thicknesses that ranged from around 1 cm at the snow surface to 50 cm at the bottom of the sea ice. We used measured snow and ice temperature profiles to initialize the model at location A. The measured thickness of the 2-year ice was 2.4 m on April 30, 1956, and the temperature of the lowest node (2.3 m beneath the sea ice surface) was −1.8°C. Temperature measurements at this location ceased for the summer on June 24, 1956, and resumed again on November 1, 1956. Only snow temperature profiles were available to initialize the model at location B. We estimated initial ice temperatures by assuming a thickness of 3 m, a bottom temperature of −1.8°C, and a profile shape similar to that in the 2-year ice. There were several breaks in the thermocouple record at location B when the array was moved. Repositioning the array caused an apparent loss of 8 cm of snow on June 13 (day 165). Between July 18 and August 27 the array was installed in a melt pond.

Estimates of initial snow density at both locations A and B ranged from 150 kg m^{-3} at the snow surface to 400 kg m^{-3} at the snow-ice interface, in general agreement with values in Table 2, which shows composite profiles by snow types observed on NP-22 [*Radionov et al.*, 1996]. We used a salinity of 0.5 psu at the top of the sea ice; for the remaining ice, we used the multiyear salinity profile for hummocked areas compiled by *Cox and Weeks* [1974]. This predicted salinities of 3.3 and 3.8 psu at the lower ice surface at locations A and B, respectively.

4.2. Snow Accumulation

Figure 7 shows measured and simulated snow depth at locations A and B. For comparison, we show two additional snow depth records from NP-4: a second record above 2-year ice and a record near the meteorological instruments. The latter contains daily averages of measurements at three snow stakes at the corners of a 25 m square. Figure 7 shows that there was considerable variability in snow depth among the locations. For example, the snow stake square accumulated over twice the snow of location B. The depth record of the latter contains several spikes, indicating wind scouring. The largest spread in accumulation among the four locations coincided with the two major snow storms of the winter: between October 26 and 29, 1956 (days 300 to 303) and between February 25 and 27, 1957 (days 56 to 58). Both of these produced low-density snow that would be subject to blowing and drifting. *Radionov et al.* [1996, Figure 5] confirm that such variability in snow depth over Arctic sea ice is not unusual, as do *Buzuev and Dubovtsev* [1978] and *Buzuev et al.* [1979].

To correctly predict temperature profiles, SNTHERM needs to accurately simulate the observed snow depth at locations A and B. Thus for NP-4, SNTHERM computes not only snow accumulation during storms but also erosion and drifting caused by the wind. We first corrected the measured precipitation using a combination of the procedures described by *Yang et al.* [1995] and *Struzer and Bryazgin* [1971], appropriate, for low-to-moderate and high wind regimes (Figure 8). Table 3 shows monthly raw precipitation in millimeters of snow–water equivalent (SWE) and precipitation corrected for collection error. Wind is the predominant factor in the correction. For low-to-moderate winds, collection efficiency decreases with wind speed; while at higher speeds, snow increasingly blows into the gauge and registers as false precipitation. Figure 8 shows a provisional interpolated curve that we used for a wind correction.

We also corrected the precipitation gauge for wetting error (0.1 mm SWE per observation) and for evaporation from the gauge. We concur with *Aaltonen et al.* [1993] that evaporative losses are significant in the spring and early summer. We did not, however, find a correction procedure in the literature and therefore arbitrarily estimated the gauge evaporation losses to be 50% of the surface evaporative losses that we compute with (25). This procedure predicted evaporation losses of around 4

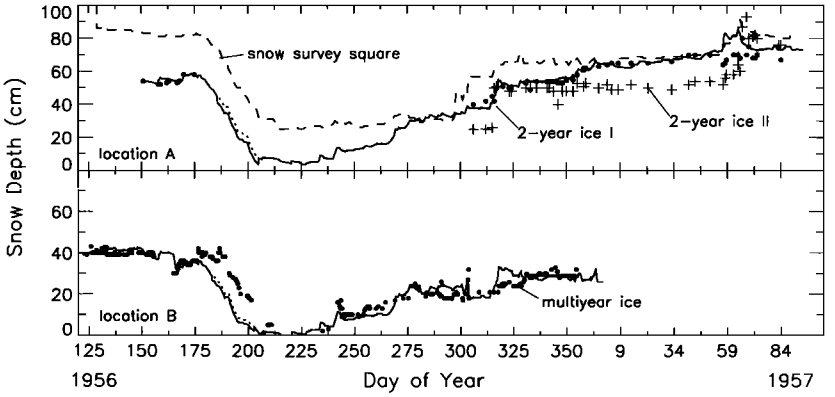

Figure 7. Simulated (line) and observed (solid circles) snow depth at locations A and B between April 30, 1956 and April 4, 1957, at NP-4. The dotted line represents the combined depth of snow and basal ice. The pluses show observed depth at another site on 2-year ice, and the dashed curve shows average depth from the snow survey square near the meteorological instruments.

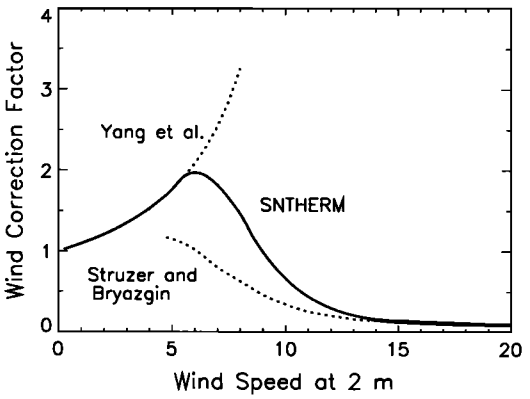

Figure 8. Wind correction factor (corrected precipitation/gauge reading) for wind speed at a gauge height of 2 m. The lines show corrections according to *Yang et al.* [1995] and *Struzer and Bryazgin* [1971] and the combined correction that we applied to the NP-4 data.

mm SWE per month for May through August, with a maximum loss of 6.9 mm in June.

Using the corrected precipitation rate and new-snow density computed from (14), SNTHERM closely replicated snow depth at location A through January 31, 1957 (Figure 7) and required no snow advection adjustment. For the remainder of the data series, we eroded the snowpack to reproduce the correct depth. This was done by assuming a fractional stress gradient in (16) of 0.0018 m^{-1} after January 31, 1957. At location B, the wind-scoured site, we assumed a fractional stress gradient of 0.0012 m^{-1} for the entire data series. According to this prediction, wind eroded 74% of the new snow at location B from October to December 1956. The modeled depth at location B generally reproduces the observed erosion spikes. Simulated threshold friction velocities during this period ranged from 0.20 m s^{-1} for new snow to 0.48 m s^{-1} for snow 18 days old, exposed by erosion of loosely bonded, upper snow layers. The model eroded less snow in the spring and summer when the simulated threshold was higher. The last two rows in Table 3 show monthly estimated accumulation at the two locations, computed as precipitation minus SWE of wind-eroded snow.

4.3. Snow Compaction and Densification

Except during periods of melting or wind erosion, short-term "dips" in the modeled depth record in Figure 7 result from compaction and are particularly noticeable in fresh snow. Wind compaction decreases snow depth at location A by up to 15% during November and December 1956. During the summer, both compaction and melting cause decreases in snow depth. There is also an apparent loss of snow when a basal ice layer forms at the snow-ice interface, in effect, shifting the interface. We arbitrarily assume that snow becomes ice when its density exceeds 820 kg m^{-3}. This basal layer forms because the freezing point of rain and meltwater is above the equilibrium temperature of the snow-ice interface. The dotted lines in Figure 7 show the combined height of snow and basal ice.

Figure 9 shows simulated average snow density at locations A and B, overlaid with observations from other NP stations with drift tracks in the vicinity of NP-4 in 1956–1957. Remember that there were no snow density measurements at NP-4. Simulated density in the spring of 1956, 310 to 340 kg m^{-3}, is in the midrange of observed values. Density increases with the onset of melting; our simulated values are consistent with "wet and melting" snow in Table 2. Large discontinuities during the melting season are artifacts of the nodal discretization scheme in SNTHERM; that is, discontinuous drops in density occur when a node is lost to basal ice; more gradual decreases coincide with falls of fresh snow. Discontinuous increases occur in late July and August when basal ice loses density through melting and is reclassified as snow. After the summer, 5 cm of old snow or firn remained at location A, giving it a higher overall density than location B. The snowpack gradually densifies over the winter. Modeled density at both locations is, for the most part, in the midrange of observations, lending support to SNTHERM's densification methods. Because of the large fall of light snow in late February 1957, SNTHERM predicts a somewhat low average density of 303 kg m^{-3} at the end of the simulation.

4.4. Snow Temperature Profiles

We used the observed snow depths and temperature profiles to test SNTHERM's ability to predict energy exchanges, both within the snow and sea ice and between the surface and the atmosphere. Figures 10 and 11 show modeled and observed temperature traces at various depths in the snow and ice at locations A and B. Data at location A were available only between May 30 and June 24 and after November 1; we present these segments separately in Figure 10. At location B, thermocouples were frequently repositioned during the summer to accommodate the melting snowpack; we note these changing positions in the caption to Figure 11. The top plot in that figure shows snow surface temperature.

The spring segment of the simulation at location A and the data agree very well for the three lowest traces and fairly well for the higher levels (left-hand portion of Figure 10). Predicted temperatures are lower than observations between June 7 (day 159) and June 13 (day 165), but we note that some of the measured temperatures were above 0°C and thus cannot be correct.

Table 3. Precipitation and Estimated Accumulation in Millimeters of Snow–Water Equivalent (SWE) at NP-4, May 1956 to March 1957

	Jan.	Feb.	March	April	May	June	July	Aug.	Sept.	Oct.	Nov.	Dec.
					Precipitation							
Raw	10.7	14.0	11.3	...	4.5	13.1	15.4	18.4	12.4	25.9	26.5	15.9
Corrected	17.6	26.6	22.7	...	16.4	35.8	28.6	34.2	23.8	38.0	50.7	31.0
					Estimated Accumulation							
Location A	17.6	21.2	3.7	...	...	35.8	28.6	34.2	23.8	38.0	50.7	31.0
Location B	...	...	...	...	10.7	29.6	28.6	30.7	19.5	5.2	24.0	2.4

The last two rows show the effects of our wind erosion parameterization (16).

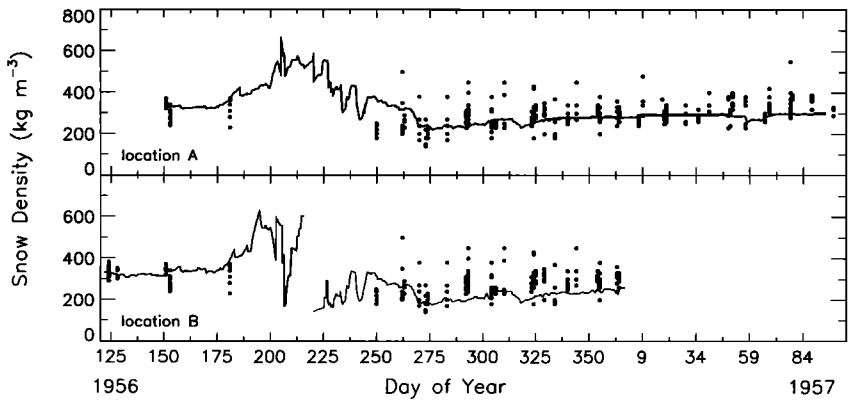

Figure 9. Simulated average snow density at locations A and B on NP-4 between April 30, 1956 and April 4, 1957. The dots are observations from other NP stations with drift tracks in the vicinity of NP-4 (87°N, 180° on April 1, 1956, to 86°N, 3°W on April 4, 1957) [*NSIDC*, 1996].

Results for the spring from location B (Figure 11) are somewhat inconclusive. There is fair agreement for the surface temperature (measured with an alcohol thermometer), but modeled temperature traces in the snow between May 3 (day 124) and June 4 (day 156) are above the observations. The observed temperatures in the snow also show short-term fluctuations even at depth; while in the modeled profile, variability in the surface forcing damps out with depth. Because the observed thermocouple profiles all tracked air temperature, we conclude that either this location was prone to wind pumping or the measurements were compromised. No similar profiles showing so little damping in temperature variation with depth were observed at NP-4.

CWTs were reinstalled for the winter on November 1, 1956

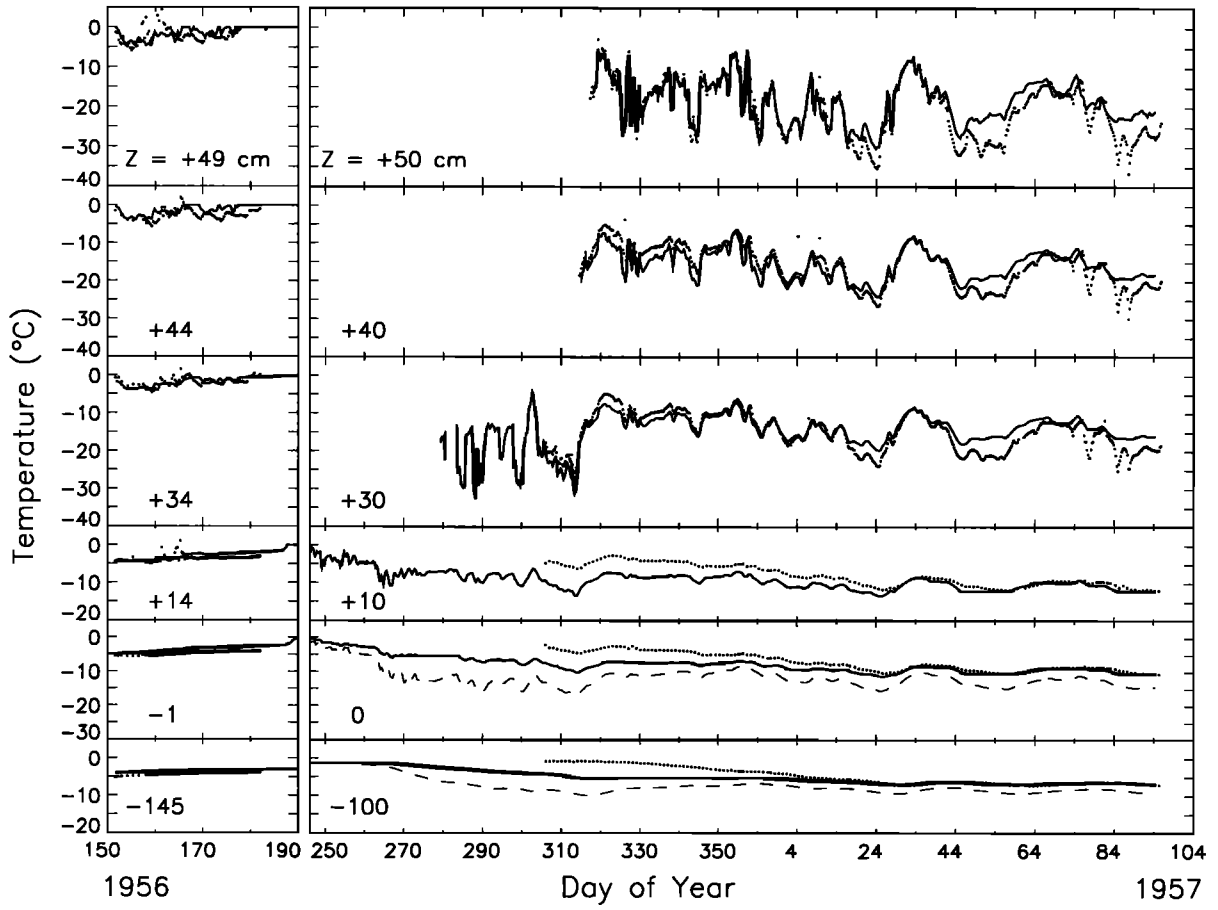

Figure 10. Modeled (line) and observed (dots) temperature traces at various depths in the snow and ice at location A on NP-4 between May 30, 1956 and April 4, 1957. The snow-ice interface is 0 cm; so plus heights are in snow, and minus heights are in sea ice. In the two bottom panels, we show as dashed curves an alternative simulation with the new-snow density set at 330 kg m^{-3}.

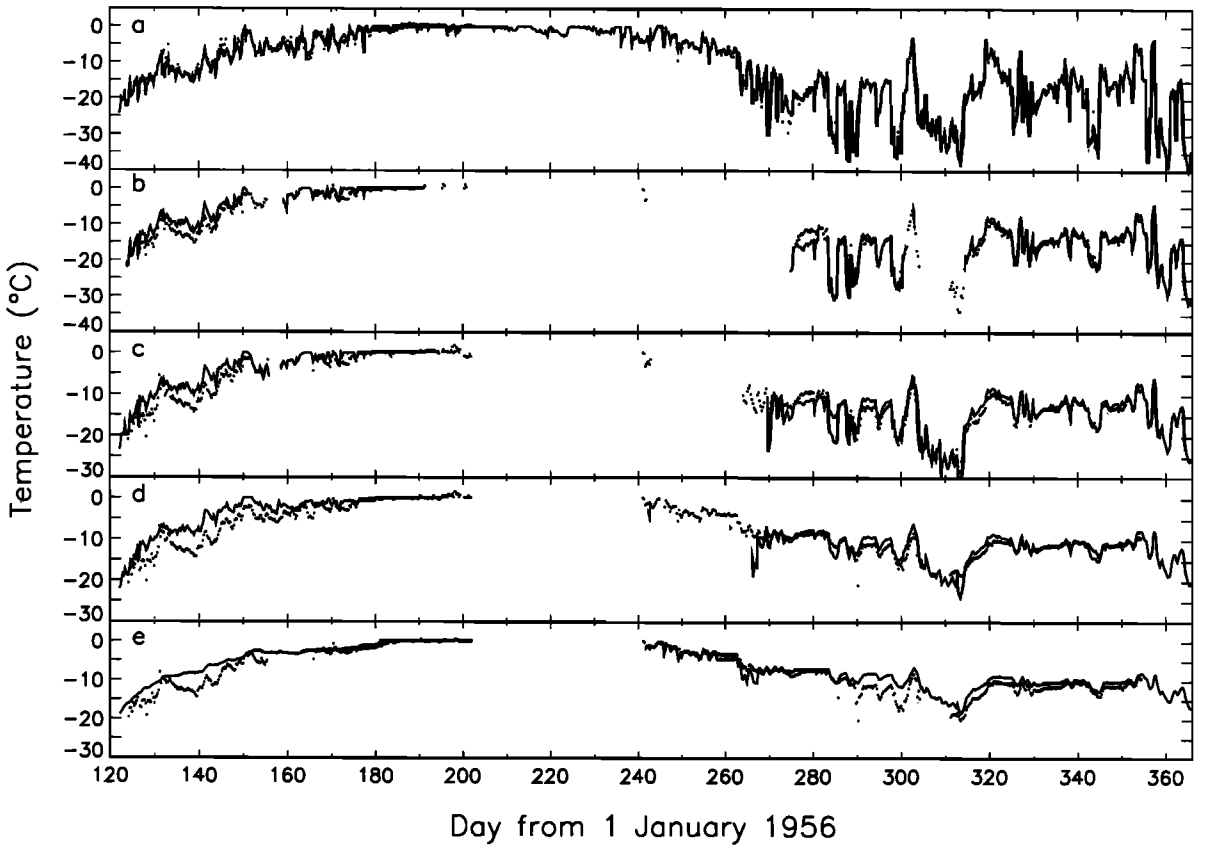

Figure 11. Modeled (line) and observed (dots) temperature traces at various depths in the snow at location B on NP-4 between April 30, 1956 and December 31. The position of the thermocouples above the snow-ice interface in Figures 11b, 11c, 11d, and 11e are as follows: day 121, b = 39 cm, c = 37 cm, d = 34 cm, e = 9 cm; day 160, b = 30 cm, c = 28 cm, d = 18 cm, e = 5 cm; day 190, b = 29 cm, c = 25 cm, d = 20 cm, e = 10 cm. Thermocouple b was again lowered by 9 cm and 3 cm on days 195 and 200, respectively. On day 241, thermocouples were reinstalled at the levels b = 20 cm, c = 15 cm, d = 10 cm, e = 5 cm. The thermocouple in Figure 11a is at the snow surface. Observations are not available after December 19, 1956.

(day 306), at location A. The right-hand side of Figure 10 shows modeled and observed temperatures at various levels in the ice and snow for a simulation running continuously since May 30, 1956. The modeled and observed traces near the surface agree well, but SNTHERM underpredicts the temperature deeper in the snow and in the ice. The observed ice surface temperature on November 1 (day 306), for instance, is −3°C compared to −8°C for the simulation. Considering that the atmosphere had been very cold since mid-September, we are surprised that the ice remained this warm and suspect that meltwater collected at this location. The second 2-year ice array (corresponding with depth record II in Figure 7) showed an interfacial temperature of −12.8°C at this time, and the +5 cm thermocouple at location B read −18.6°C, corroborating that location A was unusually warm.

To provide a more meaningful test of SNTHERM's ability to simulate in-depth temperatures, we reinitialized the run with CWT data from November 1. Figure 12 shows modeled and observed temperatures at various depths in the snow and ice for this simulation. Considering the large swings in temperature at the surface, SNTHERM tracks the CWT readings remarkably well. Simulated traces have the correct damping of amplitude with depth, and the temperature trends over time show little bias. We attribute the overprediction in March to uncertainties in simulated snow depth following the storm of February 25–27; the simulated snow cover is most likely too deep.

The winter segment of Figure 11 once again shows good agreement with data, and the overall characteristics of the traces are predicted correctly. Thinner snow cover at this site did not provide the ice with the insulation that location A had. For instance, the +10 cm temperature trace in Figure 10 (i.e., location A) is almost 10° warmer than the +10 cm trace in Figure 11e and is much more damped.

Maykut and Untersteiner [1971] conclude that variations in snow depth have little effect on the average equilibrium thickness of Arctic sea ice, except when the annual depth exceeds 70 cm. Although a thinner snow cover promotes greater ice accretion in the winter, opposing effects promote greater ice ablation in the summer. They did not examine the effect of snow density on snow and ice temperatures; in fact, the sea ice models of *Maykut and Untersteiner* [1971] and *Ebert and Curry* [1993] assume a homogeneous snow cover with a constant density of 330 kg m^{-3} in the winter and 450 kg m^{-3} in the summer.

Fresh, low-density snow is a much better insulator than denser snow, as reflected in the ρ_s^2 dependence of thermal conductivity in (9). For instance, k_t for new snow with densities predicted by (14) could be an order of magnitude less than for snow having a density of 330 kg m^{-3}. The two bottom traces in

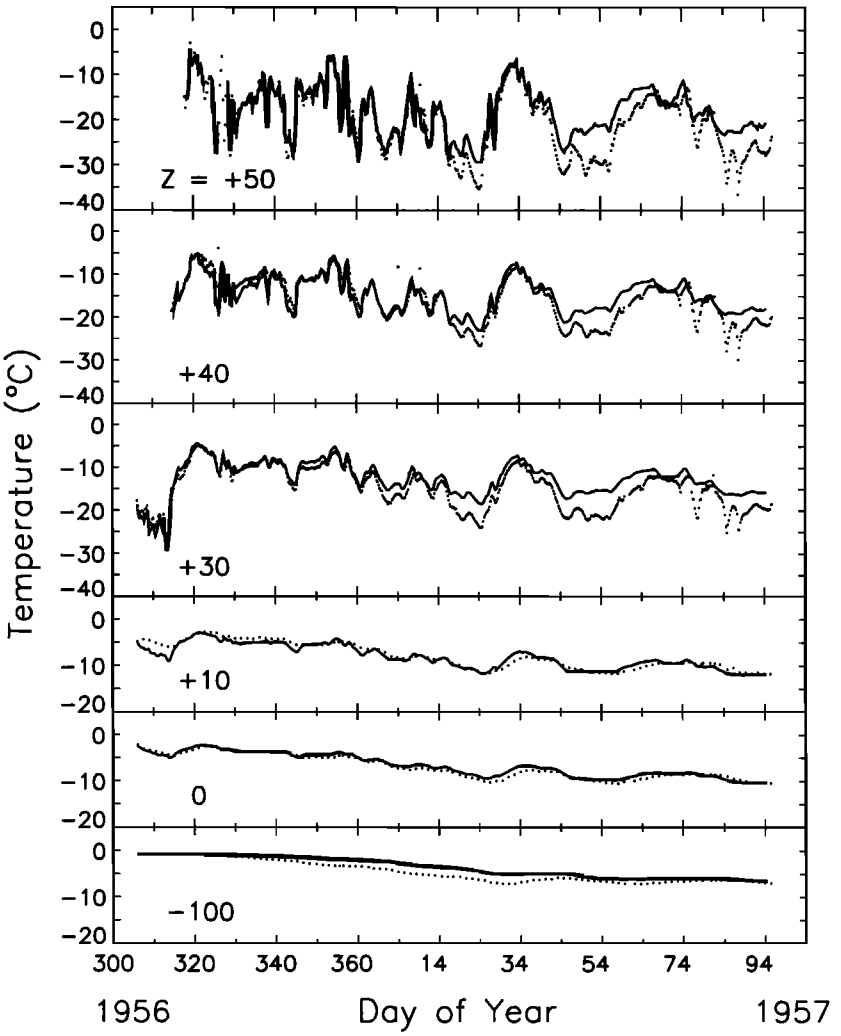

Figure 12. Modeled (line) and observed (dots) temperature traces at various depths in the snow and sea ice at location A on NP-4 between November 1, 1956 and April 4, 1957. The snow-ice interface is designated 0 cm.

Figure 10 show an alternative simulation in which we use a constant new-snow density of 330 kg m^{-3} and disable the compaction routine in SNTHERM. We increase the precipitation rate to match the observed snow depth. In this case, the ice surface temperature in the fall is up to 8°C below the baseline simulation. For the same assumed density, similar overcooling of the ice occurred at location B. Compared with observations [*Untersteiner*, 1961], *Maykut and Untersteiner*'s [1971] model cooled the ice too rapidly in the fall, perhaps, in part, because the assumed thermal conductivity was too high. More realistic snow densities could reduce predicted ice accretion in the fall.

4.5. Snow Ablation and Subsurface Melting

Diurnal melting on NP-4 in 1956 began around June 18 (day 170). After June 28 (day 180) the snow cover melted rapidly, losing about 5 mm of SWE per day through the end of July (day 213). *Yanes* [1962] and *Lindsay* [1998] corroborate these dates. A maximum runoff of 17 mm/d occurred on July 9 (day 191). Figure 7 shows close agreement between modeled ablation rates at the two locations and the available snow depth records.

Table 4 shows simulated mass balance components for the snow cover and sea ice. Values for May are from location B with no blowing snow adjustment; other values are from location A. The monthly change in millimeters of SWE equals the monthly precipitation minus evaporation and liquid water runoff, as predicted by (1). Table 4 shows surprisingly high evaporative losses for this period; 19% of the runoff and 34% of the total precipitation. For comparison, we include in Table 4 observations of mean and maximum melting and basal ice formation over 2-year ice at NP-4 [*Nazintsev*, 1963]. Simulated total melting is in the range reported by *Nazintsev* [1963]. From this result and the good agreement between modeled and observed ablation rates (Figure 7) we conclude that SNTHERM accurately estimates the surface energy fluxes.

Because we use a very simple sea ice model, our predictions of basal ice thickness and sea ice melting are less certain. *Nazintsev* [1963] and the CD-ROM documentation [*NSIDC*, 1996] clearly establish that basal ice forms, particularly under snow with a maximum depth exceeding 20 cm. We believe, however, that the basal ice thickness predicted by SNTHERM is too high, most likely because of the way we drain water at the snow-ice interface. In reality, gravitational flushing of the sea ice by meltwater and upward suction of the brine into the snow

Table 4. Mass Balance Components at North Pole 4 (1956) in Millimeters SWE

	Change in Snow Cover	Snowfall	Rain	Evaporation	Runoff	Snowmelt	Basal Ice Formed	Sea Ice Melt
May	8.1	16.4	0.0	8.3	0.0	2.3		19.7
June	21.0	23.8	12.0	14.5	0.3	3.5		16.7
July	−161.5	8.1	20.5	8.0	182.1	147.6	40.0	216.5
August	5.4	22.0	12.2	8.1	20.7	9.8		21.6
Totals	−127.0	70.3	44.7	38.9	203.1	163.2	40.0	274.5
Observed mean*						140.0	20.0	70.0
Observed max*						220.0		280.0

**Nazintsev* [1963].

[*Barber et al.*, 1995] should reduce the salinity and temperature gradients across the snow-ice interface, especially late in the melt season. Most likely, basal ice forms only in early July and under deeper snow covers, where solar radiation cannot penetrate.

SNTHERM melted 275 mm of sea ice, considerably above the average of 70 mm reported by *Nazintsev* [1963] but below his maximum of 280 mm. Heat from the excess basal ice that formed in the simulation can account for up to 20 mm of melted ice. We note that the sea ice melting predicted by SNTHERM implies enlargement of the brine pockets, whereas observed melting reflects surface thinning of the ice flow.

Figure 13 compares measured and simulated temperature profiles between 2200 UTC on June 17 (day 169) and 0400 UTC on June 19 (day 171). Simulated profiles show temperature elevated by up to 5°C at depths of 5 to 10 cm below the surface. Similar "U-shaped" profiles predominated throughout the spring, the result of subsurface absorption of solar radiation. A similar phenomenon occurs in seasonal, temperate snow covers [*Koh and Jordan*, 1995] but is more pronounced there because the snow is less dense and a poorer conductor of heat. A persistent zone of subsurface melting developed after June 28 (day 180) at NP-4. The surface was also melting during this period, but it intermittently refroze through radiative cooling whenever the sky cleared.

4.5. Turbulent Exchange

Figure 14 characterizes the stability of the atmospheric surface layer at NP-4 using 3-hourly values of the bulk Richardson number Rb. Rb defines stability in terms of meteorological observations at one level and surface values of temperature and specific humidity:

$$Rb \equiv \frac{gz\left(\dfrac{T_r - T_0}{\bar{T}} - 0.61(Q_r - Q_0)\right)}{U_r^2}. \qquad (34)$$

Rb has the same critical limits for stable stratification as Ri: 0.2 and 1.43 for the log-linear and Dutch formulations, respectively. Values of Rb have been truncated above 1.43 and below −1.43. Thus truncated values for the stable case represent conditions when, according to the Dutch formulation, turbulent transfer ceases.

Because of consistently high winds, near-neutral conditions ($-0.02 \leq Rb \leq 0.02$) prevailed at NP-4. Departures from neutrality coincided with low wind speeds and tended toward unstable stratification prior to late August (day 240) and toward stable stratification after that. A transition in the radiation balance from positive to negative occurred roughly at the same time (Figure 15). Comparing the surface and air temperatures in Figure 6 corroborates these general trends. During the winter, Rb is between the log-linear and the Dutch formulation limits (0.2 and 1.43) a significant part of the time. Using the log-linear function would erroneously predict the cessation of turbulent heat exchange and lead to excessive cooling of the snow surface during these periods.

Figure 15 shows daily averages of radiation and turbulent fluxes between April 30, 1956 and April 4, 1957. We compute longwave radiation with (23) and the turbulent fluxes with (24) and (25). We display the turbulent fluxes with a sign change, so positive fluxes in all panels represent heat gains to the snow cover. Turbulent fluxes were close in magnitude during May and June and predominantly upward, thus cooling the surface. Sensible heat exchange dropped to near zero over the melting snow of July and August. Figure 6, which shows air temperatures close to 0°C throughout this period, corroborates this result. We attribute this small sensible heat flux to the equili-

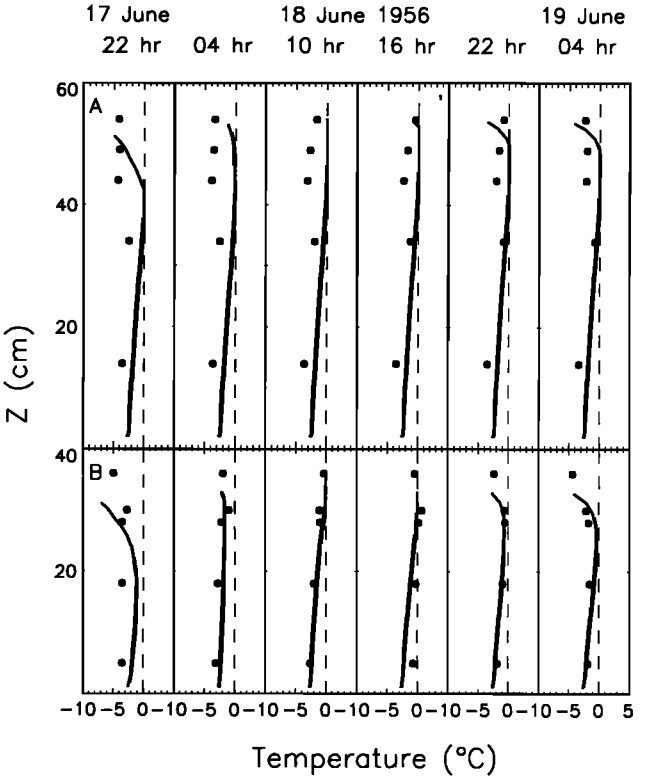

Figure 13. Modeled (line) and observed (dots) snow temperature profiles at locations A and B between 2200 UTC on June 17 and 0400 UTC on June 19, 1956.

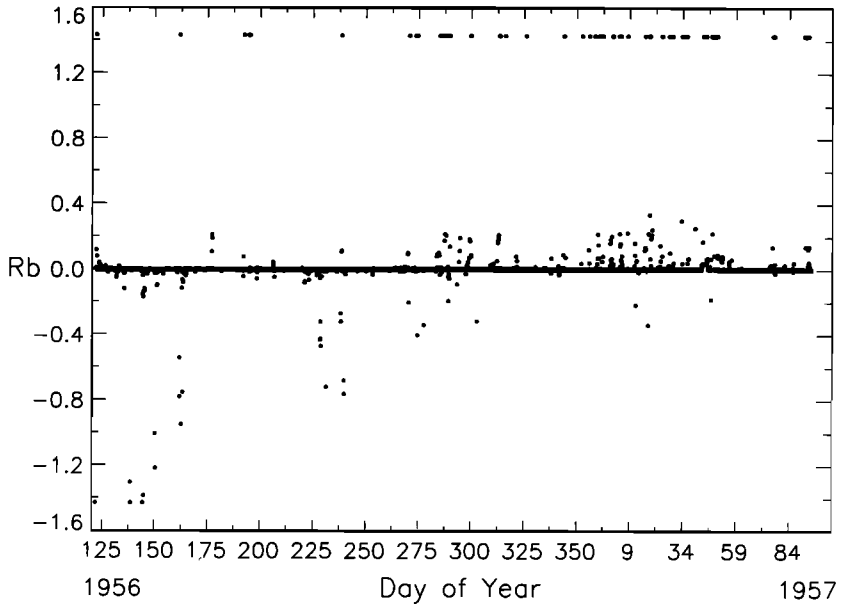

Figure 14. Three-hourly bulk Richardson number (Rb) between April 30, 1956 and April 15, 1957, at NP-4. Values above 1.43 and below −1.43 have been truncated.

brating presence of a heavy cloud cover [cf. *Makshtas et al.*, 1998]. By contrast, the snow surface continued to lose heat via evaporation throughout the melt season. This is consistent with Figures 4 and 5, which show near-zero sensible heat fluxes and positive latent heat fluxes at neutrality.

Figure 15 shows a negative radiation balance after September 11 (day 255) and simultaneously the appearance of positive spikes in the sensible heat flux, which increase in magnitude over the winter. As prescribed by (23), the largest longwave radiation losses occurred under cloudless skies. Losses were

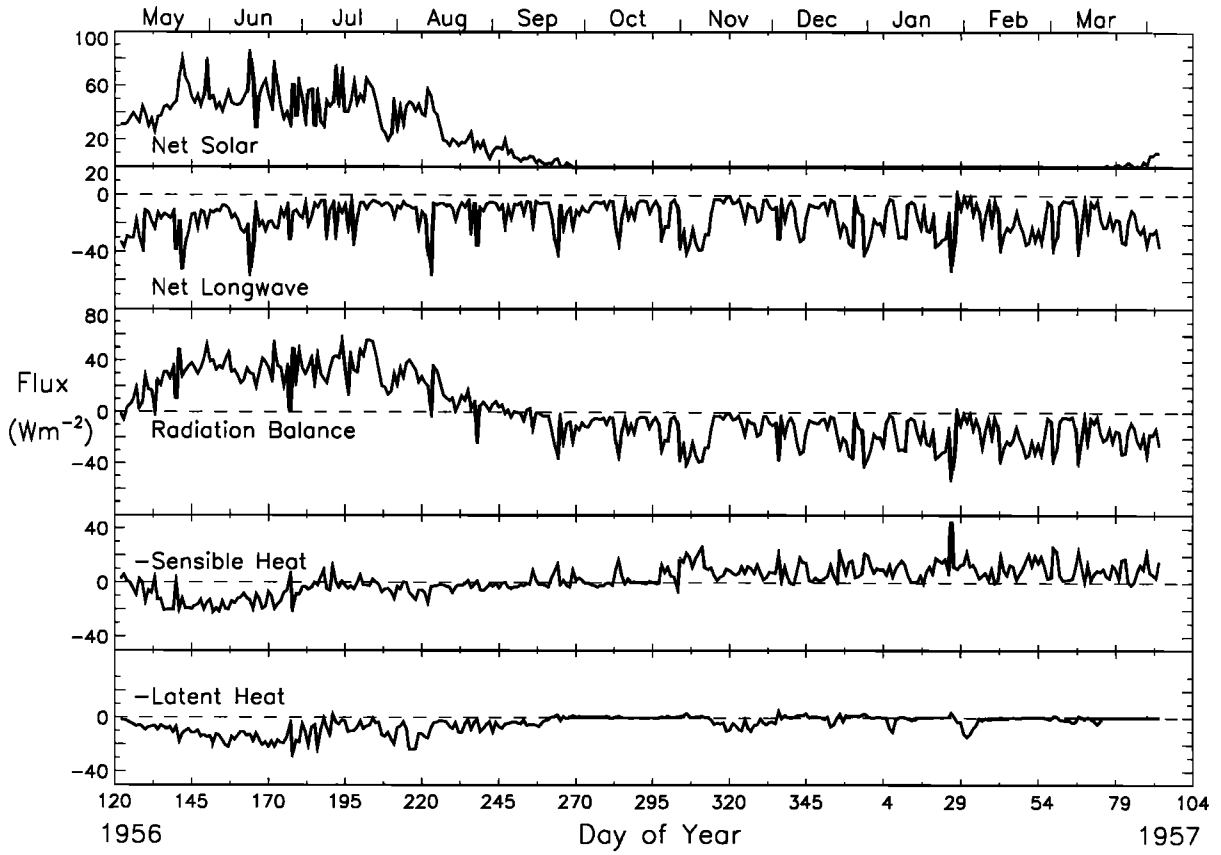

Figure 15. Daily averages of net solar radiation, net longwave radiation, radiation balance, and the negatives of the sensible and latent heat fluxes at NP-4 between April 30, 1956 and April 4, 1957.

Table 5. Monthly Averages of Sensible and Latent Heat Fluxes

	SNTHERM		*Nazintzev* [1964]		Others*	
	F_{sens} W m^{-2}	F_{lat} W m^{-2}	F_{sens} W m^{-2}	F_{lat} W m^{-2}	F_{sens} W m^{-2}	F_{lat} W m^{-2}
May	10.6	8.8	9.4	3.0	7.9	7.0
June	12.4	15.8	3.6	5.2	7.8	10.0
July	1.9	8.2	2.8	4.1	2.4	7.5
August	3.9	8.5	1.3	1.3	4.5	5.5
September	−0.4	2.3	1.9	0.0	3.7	1.3
October	−2.9	−0.4	−0.9	0.0	−1.5	−0.5
November	−10.3	3.4	−4.5	−0.5	−6.5	−1.3
December	−8.9	−0.9	−8.0	−0.6	−4.9	0.2
January	−11.5	1.3	−10.5	−1.4	−7.0	0.0
February	−11.1	0.7	−10.6	−0.9	−7.0	0.2
March	−8.3	0.4	−7.3	−0.6	−7.0	0.3

**Makshtas* [1984] for F_{sen} in December through March; an average of *Doronin* [1963] and *Badgley* [1966] for the remaining values.

primarily compensated by sensible heat exchange and by upward conduction of heat through the snow and sea ice, as *Makshtas et al.* [1998] also found over Antarctic sea ice. For example, the large positive spike in sensible heat flux on January 26, 1957, counteracted the negative spike in net radiation, the result of clearing skies (see Figure 6). Wind speeds were moderately high for this day, averaging 7 m s^{-1}. Latent heat exchange was small during the winter because saturation vapor pressure decreases exponentially with temperature.

Table 5 compares SNTHERM monthly averaged fluxes to computations by *Nazintzev* [1964], also for NP-4. Nazintzev's fluxes were not corrected for stability and thus would be biased low for the unstable regime and high for the stable regime. The magnitude of Nazintzev's computations for the summer are generally 2 to 3 times less than SNTHERM's; only part of this can be attributed to the stability correction. The sensible heat fluxes agree particularly well for the winter. Latent heat fluxes computed both by SNTHERM and by Nazintsev are small and inconsistent in direction. We attribute this, in part, to our having only monthly climatological humidity data for the winter. We do note, however, that asymmetry in the stability correction favors an upward latent heat flux. The F_{lat} values in Table 5 and the generally downward spikes in the latent heat panel in Figure 15 are evidence of this tendency.

For further comparison, we show in Table 5 an average of fluxes computed by *Doronin* [1963] and *Badgley* [1966] and by *Makshtas* [1984] for sensible heat in the winter on NP-23. They all used a flux-gradient method to calculate F_{sens} and F_{lat}, employing measurements at two levels rather than modeling the surface values as in (24) and (25). These values agree fairly well with ours and corroborate that SNTHERM estimates the fluxes correctly.

The *Andreas and Cash* [1996] study of the Bowen ratio (F_{sens}/F_{lat}) over saturated surfaces, such as snow-covered sea ice, provides an additional way of checking the SNTHERM fluxes in Table 5 for consistency. They show how to estimate the Bowen ratio from surface temperature alone for the three dominant heat flux regimes described in section 2.4. In unstable stratification, with the exception of July, monthly averaged estimates using their method agree well with SNTHERM.

In January 1957 there were several periods of very stable stratification. These provided an opportunity to investigate the effects of the windless exchange coefficient in (24). The left-hand panel in Figure 16 shows measured surface temperature and our predictions of it using computed longwave radiation and (line a) the Dutch formulation and a windless coefficient of $E_0 = 1.0$, (line b) the Dutch formulation and no windless coefficient, (line c) the log-linear formulation and no windless coefficient. Lines a′, b′, and c′ in the figure are the same as lines a, b, and c except we use measured longwave radiation. Between January 18 and 21 and between January 22 and 25 the three temperature simulations using computed longwave radiation are all in closer agreement with observations than those using measured radiation. Within these subgroups the Dutch formulation with a windless coefficient provides the best estimate, and the log-linear formulation without a windless coefficient provides the worst.

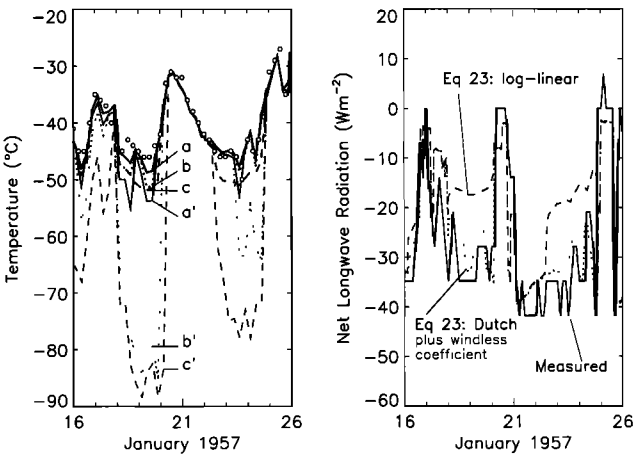

Figure 16. (left) Measured surface temperature (open circles) and SNTHERM simulations between January 16 and 26, 1957, at location A. The three top traces use computed longwave radiation and (line a) the Dutch formulation and a windless coefficient of $E_0 = 1.0$ (solid line), (line b) the Dutch formulation and no windless coefficient (dots), and (line c) the log-linear formulation with no windless coefficient (dashes). Plots a′, b′, and c′ are the same, except we use measured longwave radiation. (right) Measured (solid line) and computed net longwave radiation from equation (23). Dashed and dotted curves show computed longwave radiation when the turbulent fluxes are computed, respectively, with the log-linear formulation and with the Dutch formulation and a windless coefficient.

The low bias of up to 35°C in run c′ (compared with run c) does not result from poor radiation data. Rather, this bias results from the manner in which emitted longwave radiation is handled. In lines a, b, and c we compute emitted radiation from the Stefan-Boltzmann equation, which provides an additional constraint on surface temperature not available when measured net radiation is used. The right-hand panel in Figure 16 shows that measured and computed values of net radiation are actually quite close when the turbulent fluxes are computed with Dutch formulation and a windless coefficient. This close agreement supports the accuracy of both radiation measurements and cloud observations at NP-4 as well as the validity of (23). By contrast, computed net radiation is too high when we use the log-linear formulation. We contend that using the log-linear formulation during overly stable stratification leads to computational errors in both the radiative and the sensible heat fluxes; the former estimates are too high and the latter are too low.

For clarification, we examine the inversion of January 18–20. In run c the snow surface decouples from the atmosphere early on January 18 and remains decoupled (i.e., the turbulent fluxes are zero) for over 2 days. The onset of decoupling coincides with a rapid decrease in cloud cover and decreasing air temperature, as is typical of other strong inversions during January. The 8-m wind speed was 1–2 m s^{-1}, but in other situations, decoupling occurred at speeds as high as 3 m s^{-1}. By contrast, the atmosphere in run a is nonturbulent only until 1000 on January 18, after which full turbulence resumes. During the nonturbulent period the windless coefficient maintains an average sensible heat exchange of around -6.0 W m^{-2}. At midnight on January 18, net longwave radiation and sensible heat fluxes for run a are -32.7 and -17.9 W m^{-2}, respectively; for run c they are -17.8 and 0.0 W m^{-2}, respectively. Measured net longwave at this time was -34.8 W m^{-2}. We contend that the snow surface in run c cools excessively because there is no compensating sensible heat flux. We therefore propose that the Dutch formulation in combination with a windless exchange coefficient provides the most realistic estimates of the sensible heat flux during stable stratification. When net longwave measurements are used to drive snow and sea ice models, it is particularly important to include a windless coefficient or an alternative means of maintaining exchange with the atmosphere to avoid underpredicting the surface temperature, as occurs in cases b′ and c′.

5. Conclusions

We modified a one-dimensional mass and energy balance model developed for snow-covered ground (SNTHERM) to handle sea ice and polar snow. Our treatment of in-snow processes is more complex than existing sea ice models, which assume a homogeneous snow cover and simulate only thermal exchanges. By contrast, SNTHERM builds a stratified snow cover with realistic snow properties and handles internal exchanges of vapor, liquid water, and solar radiation. We force SNTHERM with 3-hour meteorological data from North Pole 4 interpolated to hourly time steps. We thereby investigate in-snow processes occurring on a shorter timescale than the 8-hour time step used by existing sea ice models.

Using this modified version of SNTHERM, we successfully simulate temperature profiles in snow and sea ice between May 1956 and April 1957 for two locations on NP-4. Modeled temperature traces have the correct damping of amplitude fluctuations with depth and show the proper trends over time. We show that both snow depth and density influence the temperature structure. Sea ice models which assume a constant density, for example 330 kg m^{-3}, may overpredict ice growth in the fall. Large variations in snow depth and density, the result of blowing and drifting snow, lead to variations in the surface heat budget over fairly small horizontal distances. We introduce a wind transport function that erodes or accumulates surface snow in response to a specified wind stress gradient. Such heterogeneities in the surface heat and mass budget deserve more study and can be simulated, in part, with the wind transport function.

We examine mass, thermal, and radiative exchanges during the summer melting season on NP-4. Simulated spring and summer profiles in the snow show a sustained subsurface temperature maximum resulting from absorbed solar radiation. In-snow temperature profiles at location B and, to a lesser degree, at location A confirm the existence of this subsurface maximum. Melting is primarily driven by solar insolation rather than by sensible heat gain, which is a more significant component in temperate regions. The timing and rate of modeled snow ablation agree closely with observations; total amounts of snow melting, sea ice melting, and basal ice growth are in the range of values reported by *Nazintsev* [1963]. We believe, however, that SNTHERM simulates excessive basal ice growth and could be improved by letting it transport meltwater and brine across the ice-snow interface.

Observations show that the 2-m air temperature at NP-4 remained near 0°C during the summer of 1956. Simulated turbulent fluxes over the melting snow of July and August are consistent with near-neutral values shown in Figures 4 and 5 and clearly exhibit the asymmetrical effect of correcting for stability. Our simulated turbulent fluxes compare favorably with flux-gradient estimates at other NP stations and with winter estimates at NP-4. We extend the range of turbulent exchange during stable stratification by replacing the standard log-linear formula with the Dutch formulation. To our knowledge, we are the first investigators to test this relatively new parameterization with a snow model. We also introduce a windless coefficient in the bulk parameterization that allows sensible heat exchange to continue although the mean wind speed might be near zero. Physically, we assume that breaking internal gravity waves, which are common in stable boundary layers, account for this "windless" exchange. In effect, this windless coefficient prevents the air and the snow surface from decoupling. Without the coefficient, simulated surface temperatures can be unrealistically low while winter cold fronts pass. We show that it is particularly unadvisable to use the log-linear stability correction when net radiation measurements are used to drive a simulation since surface temperature can then be underpredicted by up to 40°C.

Acknowledgments. We thank the National Snow and Ice Data Center at the University of Colorado, Boulder, for providing us the CD-ROM of archived data from the Russian drifting stations. We also thank N. N. Bryazgin of the Arctic and Antarctic Research Institute for his assistance in correcting the precipitation data and R. E. Davis, W. B. Tucker, R. W. Lindsay, J. C. King, and an anonymous reviewer for their contributions to this manuscript. The Office of Naval Research supported this work through grants N0001496MP30005 and N0001497MP30002; the Cold Regions Research and Engineering Laboratory supported it under its ILIR (In-House Independent Laboratory Research) program; the Arctic and Antarctic Research Institute supported it under STP-2 AARI project 2.11, RFFI 96-07-89159, and

97-05-65926; and the National Science Foundation supported it with grant OPP-97-02025.

References

Aaltonen, A., E. Elomaa, A. Tuominen, and P. Valkovuori, Measurement of precipitation, in *Proceedings of the Symposium on Precipitation and Evaporation*, vol. 1, edited by B. Sevruk and M. Lapin, pp. 42–46, Slovak Hydrometeorol. Inst., Bratislava, Slovakia, 1993.

Anderson, E. A., A point energy and mass balance model of a snow cover, *NOAA Tech. Rep. NWS 19*, 150 pp., Off. of Hydrol., Natl. Weather Serv., Silver Spring, Md., 1976.

Andreas, E. L., A theory for the scalar roughness and the scalar transfer coefficients over snow and sea-ice, *Boundary Layer Meteorol.*, *38*, 159–184, 1987a.

Andreas, E. L., Spectral measurements in a disturbed boundary layer over snow, *J. Atmos. Sci.*, *44*, 1912–1939, 1987b.

Andreas, E. L., The atmospheric boundary layer over polar marine surfaces, *Monogr. 96-2*, 38 pp., U.S. Army Cold Reg. Res. and Eng. Lab., Hanover, N. H., 1996.

Andreas, E. L., and B. A. Cash, A new formulation for the Bowen ratio over saturated surfaces, *J. Appl. Meteorol.*, *35*, 1279–1289, 1996.

Andreas, E. L., and K. J. Claffey, Air-ice drag coefficients in the western Weddell Sea, 1, Values deduced from profile measurements, *J. Geophys. Res.*, *100*, 4821–4831, 1995.

Bader, H.-P., and P. Weilenmann, Modeling temperature distribution, energy and mass flow in a (phase-changing) snowpack, I, Model and case studies, *Cold Reg. Sci. Technol.*, *20*, 157–181, 1992.

Badgley, F. I., Heat budget at the surface of the Arctic Ocean, in *Proceedings of the Symposium on the Arctic Heat Budget and Atmospheric Circulation*, edited by J. O. Fletcher, B. Keller, and S. M. Olenicoff, pp. 267–277, *Memo. RM-5233-NSF*, Rand Corp., Santa Monica, Calif., 1966.

Banke, E. G., S. D. Smith, and R. J. Anderson, Drag coefficients at AIDJEX from sonic anemometer measurements, in *Sea Ice Processes and Models*, edited by R. S. Pritchard, pp. 430–442, Univ. of Wash. Press, Seattle, 1980.

Barber, D. G., S. P. Reddan, and E. F. LeDrew, Statistical characterization of the geophysical and electrical properties of snow on landfast first-year sea ice, *J. Geophys. Res.*, *100*, 2673–2686, 1995.

Baumann, R. J., An analysis of one year of surface layer meteorological data from the Arctic pack ice, 52 pp., M.S. thesis, Oreg. State Univ., Corvallis, 1978.

Beljaars, A. C. M., and A. A. M. Holtslag, Flux parameterization over land surfaces for atmospheric models, *J. Appl. Meteorol.*, *30*, 327–341, 1991.

Bespalov, D. P., The heat exchange between the atmosphere and the ocean in the central Arctic (in Russian), *Tr. Arkt. Antarkt. Nauchno-Issled. Inst.*, *226*, 30–41, 1959. (Translation available from the CRREL Library.)

Bilello, M. A., Regional and seasonal variations in snow-cover density in the USSR, *CRREL Rep. 84-22*, 70 pp., U.S. Army Cold Reg. Res. and Eng. Lab., Hanover, N. H., 1984.

Bogorodskii, V. V. (Ed.), *Physical Methods of Studying Ice and Snow* (in Russian), 228 pp., *Tr. Arkt. Antarkt. Nauchno-Issled. Inst.*, *326*, 1975. (Available as CRREL draft translation 539.)

Bohren, C. F., and B. R. Barkstrom, Theory of the optical properties of snow, *J. Geophys. Res.*, *79*, 4527–4535, 1974.

Brun, E., E. Martin, V. Simon, C. Gendre, and C. Coleou, An energy and mass model of snow cover suitable for operational avalanche forecasting, *J. Glaciol.*, *35*, 333–342, 1989.

Businger, J. A., A note on the Businger-Dyer profiles, *Boundary Layer Meteorol.*, *42*, 145–151, 1988.

Businger, J. A., J. C. Wyngaard, Y. Izumi, and E. F. Bradley, Flux-profile relationships in the atmospheric surface layer, *J. Atmos. Sci.*, *28*, 181–189, 1971.

Buzuev, A. Y., and V. F. Dubovtsev, Certain patterns in the distribution of snow and ice cover thickness on the Arctic seas, *Sov. Meteorol. Hydrol.*, no. 3, 44–48, 1978.

Buzuev, A. Y., I. P. Romanov, and V. E. Fedyakov, Variability of snow distribution on Arctic Ocean ices, *Sov. Meteorol. Hydrol.*, no. 9, 57–64, 1979.

Carson, D. J., and J. R. Richards, Modelling surface turbulent fluxes in stable conditions, *Boundary Layer Meteorol.*, *14*, 67–81, 1978.

Chernigovskii, N. T., and M. S. Marshunova, *Climate of Soviet Arctic Regions (Radiation Regime)* (in Russian), 155 pp., Hydrometeorol. Publ. (Gidrometeoizdat), St. Petersburg, Russia, 1965.

Colbeck, S. C., One-dimensional water flow through snow, *Res. Rep. 296*, 21 pp., U.S. Army Cold Reg. Res. and Eng. Lab., Hanover, N. H., 1971.

Colbeck, S. C., An overview of seasonal snow metamorphism, *Rev. Geophys.*, *20*, 45–61, 1982.

Colbeck, S. C., and E. A. Anderson, The permeability of a melting snow cover, *Water Resour. Res.*, *18*, 904–908, 1982.

Colbeck, S. C., E. Akitaya, R. Armstrong, H. Gubler, J. Lafeuille, K. Lied, D. McClung, and E. Morris, *The International Classification for Seasonal Snow on the Ground*, Int. Comm. on Snow and Ice of Int. Assoc. of Sci. Hydrol. and Int. Glaciol. Soc., Cambridge, England, 1990.

Colony, R. L., I. Rigor, and K. A. Runciman-Moore, A collection of sea ice trajectories in the Arctic Ocean—Preliminary report, *Tech. Memo. ARL-UW TM 4-90*, 228 pp., Appl. Phys. Lab., Univ. of Wash., Seattle, 1990.

Cox, G. F. N., and W. F. Weeks, Salinity variations in sea ice, *J. Glaciol.*, *13*, 109–120, 1974.

Doronin, Y. P., On the heat budget of the central Arctic (in Russian), *Tr. Arkt. Antarkt. Nauchno-Issled. Inst.*, *253*, 178–184, 1963. (Translated in *Soviet Data on the Arctic Heat Budget and Its Climatic Influence*, edited by J. O. Fletcher, B. Keller, and S. M. Olenicoff, pp. 193–205, *Memo. RM-5003-PR*, Rand Corp., Santa Monica, Calif., 1966.)

Doronin, Y. P., Characteristics of the heat exchange, in *Proceedings of the Symposium on the Arctic Heat Budget and Atmospheric Circulation*, edited by J. O. Fletcher, pp. 247–266, *RM-5233-NSF*, Rand Corp., Santa Monica, Calif., 1966.

Dyer, A. J., A review of flux-profile relationships, *Boundary Layer Meteorol.*, *7*, 363–372, 1974.

Ebert, E. E., and J. A. Curry, An intermediate one-dimensional thermodynamic sea ice model for investigating ice-atmosphere interactions, *J. Geophys. Res.*, *98*, 10,085–10,109, 1993.

Fairall, C. W., E. F. Bradley, D. P. Rogers, J. B. Edson, and G. S. Young, Bulk parameterization of air-sea fluxes for Tropical Ocean-Global Atmosphere Coupled Ocean-Atmosphere Response Experiment, *J. Geophys. Res.*, *101*, 3747–3764, 1996.

Fletcher, J. D., B. Keller, and S. M. Olenicoff (Eds.), *Soviet Data on the Arctic Heat Budget and Its Climatic Influence*, *Memo. RM-5003-PR*, 206 pp., Rand Corp., Santa Monica, Calif., 1966.

Glen, J. W., The physics of ice, *Monograph II-C2a*, 86 pp., U.S. Army Cold Reg. Res. and Eng. Lab., Hanover, N. H., 1974.

Godfrey, J. S., and A. C. M. Beljaars, On the turbulent fluxes of buoyancy, heat, and moisture at the air-sea interface at low wind speeds, *J. Geophys. Res.*, *96*, 22,043–22,048, 1991.

Gorshkov, S. G. (Ed.), *World Ocean Atlas: Arctic Ocean* (in Russian), vol. 3, 188 pp., Pergamon, Tarrytown, N. Y., 1983.

Gow, A. J., On the rates of growth of grains and crystals in South Polar firn, *J. Glaciol.*, *8*, 241–252, 1969.

Grenfell, T. C., and G. A. Maykut, The optical properties of ice and snow in the Arctic Basin, *J. Glaciol.*, *18*, 445–463, 1977.

Gruell, J. W., and T. Konzelmann, Numerical modeling of the energy balance and the englacial temperature of the Greenland ice sheet: Calculations for the ETH-Camp location (West Greenland, 155 m a.s.l.), *Global Planet. Change*, *9*, 91–114, 1994.

Guryanov, I. E., Thermal-physical characteristics of frozen, thawing and unfrozen grounds, in *Proceeding of the Fourth International Symposium on Ground Freezing*, edited by S. Kinosita and M. Fukuda, pp. 225–230, A. A. Balkema, Brookfield, Vt., 1985.

Halberstam, I., and R. Melendez, A model of the planetary boundary layer over a snow surface, *Boundary Layer Meteorol.*, *16*, 431–452, 1979.

Haugen, D. A. (Ed.), *Workshop on Micrometeorology*, 392 pp., Am. Meteorol. Soc., Boston, Mass., 1973.

Hibler, W. D., III, A dynamic thermodynamic sea ice model, *J. Phys. Oceanogr.*, *9*, 815–846, 1979.

Hibler, W. D., III, and S. F. Ackley, Numerical simulation of the Weddell Sea pack ice, *J. Geophys. Res.*, *88*, 2873–2887, 1983.

Hicks, B. B., Wind profile relationships from the 'Wangara' experiment, *Q. J. R. Meteorol. Soc.*, *102*, 535–551, 1976.

Hobbs, P. V., and B. J. Mason, The sintering and adhesion of ice, *Philos. Mag.*, *9*, 181–197, 1964.

Holtslag, A. A. M., and H. A. R. de Bruin, Applied modeling of the nighttime surface energy balance over land, *J. Appl. Meteorol.*, *27*, 689–704, 1988.

Hosler, C. L., D. C. Jense, and L. Goldshlak, On the aggregation of ice crystals to form snow, *J. Meteorol.*, *14*, 415–420, 1957.

Jordan, R., A one-dimensional temperature model for a snow cover: Technical documentation for SNTHERM.89, *Special Rep. 91-16*, 49 pp., U.S. Army Cold Reg. Res. and Eng. Lab., Hanover, N. H., 1991.

Kaimal, J. C., and J. C. Wyngaard, The Kansas and Minnesota experiments, *Boundary Layer Meteorol.*, *50*, 31–47, 1990.

Keeler, C. M., The growth of bonds and the increase of mechanical strength in a dry seasonal snow-pack, *J. Glaciol.*, *8*, 441–450, 1969.

Kind, R. J., Snow-drifting, in *Handbook of Snow: Principles, Processes, Management and Use*, edited by D. M. Gray and D. H. Male, pp. 338–359, Pergamon, Tarrytown, N. Y., 1981.

King, J. C., and P. S. Anderson, Heat and water vapour fluxes and scalar roughness lengths over an Antarctic ice shelf, *Boundary Layer Meteorol.*, *69*, 101–121, 1994.

King, J. C., and W. M. Connolley, Validation of the surface energy balance over the Antarctic ice sheets in the U.K. Meteorological Office Unified Climate Model, *J. Clim.*, *10*, 1273–1287, 1997.

Koh, G., and R. Jordan, Sub-surface melting in a seasonal snow cover, *J. Glaciol.*, *41*, 474–482, 1995.

Konig, G., Roughness length of an Antarctic ice shelf, *Polarforschung*, *55*, 27–32, 1985.

Konig-Langlo, G., and E. Augstein, Parameterization of the downward long-wave radiation at the Earth's surface in polar regions, *Meteorol Z.*, *3*, 343–347, 1994.

Kotlyakov, V. M., Results a of (*sic*) study of the processes of formation and structure of the upper layer of the ice sheet in Eastern Antarctica, in *Symposium on Antarctic Glaciology*, *Publ. 55*, pp. 88–99, IAHS Press, Belgium, 1961.

Kucherov, N. V., and M. S. Sternzat, The apparatus and method of investigations at stations North Pole 4 and North Pole 5 (in Russian), *Tr. Arkt. Antarkt. Nauchno-Issled. Inst.*, *226*, 5–18, 1959. (Translation available from the CRREL Library.)

LaChapelle, E., Snow layer densification, *Proj. F, Progr. Rep. 1*, 8 pp., Alta Avalanche Study Cent., U.S. Dep. of Agric. For. Serv., Wasatch Natl. For., Alta, Utah, 1961.

Laikhtman, D. L., Several regularities of the heat regime in the central Arctic (in Russian), *Tr. Arkt. Antarkt. Nauchno-Issled. Inst.*, *226*, 42–47, 1959. (Translation available from the CRREL Library.)

Launiainen, J., and T. Vihma, Derivation of turbulent surface fluxes—An iterative flux-profile method allowing arbitrary observing heights, *Environ Software*, *5*, 113–124, 1990.

Li, L., and J. W. Pomeroy, Estimates of threshold wind speeds for snow transport using meteorological data, *J. Appl. Meteorol.*, *36*, 205–213, 1997.

Lindsay, R. W., Temporal variability of the energy balance of thick Arctic pack ice, *J. Clim.*, *11*, 313–333, 1998.

Loth, B., H.-F. Graf, and J. M. Oberhuber, Snow cover model for global climate simulations, *J. Geophys. Res.*, *98*, 10,451–10,464, 1993.

Louis, J.-F., A parametric model of vertical eddy fluxes in the atmosphere, *Boundary Layer Meteorol.*, *17*, 187–202, 1979.

Lumley, J. L., and H. A. Panofsky, *The Structure of Atmospheric Turbulence*, 239 pp., Interscience, New York, 1964.

Lynch-Steiglitz, M., The development and validation of a simple snow model for the GISS GCM, *J. Clim.*, *7*, 1842–1855, 1994.

Magono, C., and C. W. Lee, Meteorological classification of natural snow crystals, *J. Fac. Sci., Hokkaido Univ., Ser. VII*, *2*, 321–362, 1966.

Makshtas, A. P., *The Heat Budget of Arctic Ice in the Winter* (in Russian), 67 pp., Gidrometeoizdat, St. Petersburg, Russia, 1984. (English translation available as Makshtas, A. P., *The Heat Budget of Arctic Ice in the Winter*, 77 pp., Int. Glaciol. Soc., Cambridge, England, 1991.)

Makshtas, A. P., E. L. Andreas, P. N. Svyashchennikov, and V. F. Timachev, Accounting for clouds in sea ice models, *CRREL Rep. 98-9*, 32 pp., U.S. Army Cold Reg. Res. and Eng. Lab., Hanover, N. H., 1998.

Marshunova, M. S., Principal characteristics of the radiation balance of the underlying surface of the atmosphere in the Arctic (in Russian), *Tr. Arkt. Antarkt. Nauchno-Issled. Inst.*, *229*, 5–53, 1961. (Translated in *Soviet Data on the Arctic Heat Budget and Its Climatic Influence*, edited by J. O. Fletcher, B. Keller, and S. M. Olenicoff, pp. 51–131, *Memo. RM-5003-PR*, Rand Corp., Santa Monica, Calif., 1966.)

Marshunova, M. S., and A. A. Mishin, Handbook of the radiation regime of the Arctic Basin (Results from the drift stations), *Tech. Rep. APL-UW TR 9413*, 69 pp., Appl. Phys. Lab., Univ. of Wash., Seattle, 1994.

Maykut, G. A., Energy exchange over young sea ice in the central Arctic, *J. Geophys. Res.*, *83*, 3646–3658, 1978.

Maykut, G. A., Large-scale heat exchange and ice production in the central Arctic, *J. Geophys. Res.*, *87*, 7971–7984, 1982.

Maykut, G. A., and N. Untersteiner, Some results from a time dependent thermodynamic model of sea ice, *J. Geophys. Res.*, *76*, 1550–1575, 1971.

McGurk, B., D. Azuma, and R. Kattelmann, Density of new snow in the central Sierra Nevada, *Proc. 56th West. Snow Conf.*, pp. 158–161, Kalispell, Mont., 1988.

Meister, R., Density of new snow and its dependence on air temperature, *Zürcher Geogr. Schriften*, No. 23, in *Proceedings of the ETH/IAHS/WMO Workshop on the Correction of Precipitation Measurements*, Eidg. Tech. Hochsch., Zurich, edited by B. Sevruk, pp. 73–79, Zurich, 1985.

Middleton, W. E. K., and A. F. Spilhaus, *Meteorological Instruments*, 3rd. ed., 286 pp., Univ. of Toronto Press, Toronto, Ontario, 1957.

Monin, A. S., and A. M. Obukhov, Basic laws of turbulent mixing in the ground layer of the atmosphere (in Russian), *Tr. Akad. Nauk SSSR, Geofiz Inst.*, *24*, 163–187, 1954. (Translation available from NTIS as AD-672723.)

Morris, E. M., H.-P. Bader, and P. Weilenmann, Modelling temperature variations in polar snow using DAISY, *J Glaciol.*, *43*, 180–191, 1997.

National Snow and Ice Data Center (NSIDC), *Arctic Ocean Snow and Meteorological Observations From Drifting Stations. 1937, 1950–1991, Version 1.0* [CD-ROM], Univ. of Colo., Boulder, 1996.

Nazintsev, Y. L., On the role of thermal processes in sea ice melting and in the transformation of the relief of multiyear ice floes in the central Arctic (in Russian), *Prob. Arkt. Antarkt.*, *12*, 69–75, 1963. (Translation available from the CRREL Library.)

Nazintsev, Y. L., Thermal balance of the surface of the perennial ice cover in the central Arctic (in Russian), *Tr. Arkt. Antarkt Nauchno-Issled. Inst.*, *267*, 110–126, 1964. (Translation available from the CRREL Library.)

Okamoto, M., and E. K. Webb, The temperature fluctuations in stable stratification, *Q. J. R. Meteorol. Soc.*, *96*, 591–600, 1970.

Overland, J. E., Atmospheric boundary layer structure and drag coefficients over sea ice, *J. Geophys. Res.*, *90*, 9029–9049, 1985.

Parkinson, C. L., and W. M. Washington, A large-scale numerical model of sea ice, *J. Geophys. Res.*, *84*, 311–337, 1979.

Patankar, S. V., *Numerical Heat Transfer and Fluid Flow*, 197 pp., Hemisphere, New York, 1980.

Paulson, C. A., The mathematical representation of wind speed and temperature profiles in the unstable atmospheric surface layer, *J. Appl. Meteorol.*, *9*, 857–861, 1970.

Perovich, D. K., The optical properties of sea ice, *Monogr. 96-1*, 25 pp., U.S. Army Cold Reg. Res. and Eng. Lab., Hanover, N. H., 1996.

Pomeroy, J. W., D. M. Gray, and P. G. Landine, The prairie blowing snow model: Characteristics, validation, operation, *J. Hydrol.*, *144*, 165–192, 1993.

Radionov, V. F., N. N. Bryazgin, and E. I. Aleksandrov, *The Snow Cover of the Arctic Basin* (in Russian), 124 pp., Gidrometeoizdat, St. Petersburg, Russia, 1996. (English translation available as Radionov, V. F., N. N. Bryazgin, and E. I. Aleksandrov, The snow cover of the Arctic Basin, *Tech. Rep. APL-UW TR 9701*, 95 pp., Appl. Phys. Lab., Univ. of Wash., Seattle, 1997.)

Rees, J. M., Internal waves in the stable atmospheric boundary layer overlying an Antarctic ice shelf, in *Fluid Physics: Lecture Notes of Summer Schools*, edited by M. G. Verlarde and C. I. Christov, pp. 329–340, World Sci., River Edge, N. J., 1994.

Rowe, C. M., K. C. Kuivinen, and R. Jordan, Simulation of summer snowmelt on the Greenland ice sheet using a one-dimensional model, *J. Geophys. Res.*, *100*, 16,265–16,273, 1995.

Schmidt, R. A., Threshold wind speeds and elastic impact in snow transport, *J. Glaciol.*, *26*, 453–467, 1980.

Schmidt, R. A., Transport rate of drifting snow and the mean wind speed profile, *Boundary Layer Meteorol.*, *34*, 214–241, 1986.

Semtner, A. J., Jr., A model for the thermodynamic growth of sea ice in numerical investigations of climate, *J. Phys. Oceanogr.*, *6*, 379–389, 1976.

Shimizu, H., Air permeability of deposited snow, *Contrib. 1053*, 32 pp., Inst. of Low Temp. Sci., Sapporo, Japan, 1970.

Stephenson, P. J., Some considerations of snow metamorphism in the Arctic ice sheet in the light of crystal studies, in *Proceedings of an International Conference on Low Temperature Science, Physics of Ice*

and Snow, pp. 725–740, Inst. of Low Temp. Sci., Hokkaido Univ., Sapporo, Japan, 1967.

Struzer, I. R., and N. N. Bryazgin, Method of computing corrections to atmospheric precipitation measurements in polar regions, *Sov. Hydrol. Selec. Pap.*, *1*, 38–47, 1971.

Tabler, R. D., C. S. Benson, B. W. Santana, and P. Ganguly, Estimating snow transport from wind speed records: Estimates versus measurements at Prudhoe Bay, Alaska, *Proc. 58th West. Snow Conf.*, pp. 51–63, Sacramento, Calif., 1990.

Treshnikov, A. F. (Ed.), *Atlas of the Arctic* (in Russian), 264 pp., Main Off. for Geod. and Cartogr. of the Counc. of Min. of the U.S.S.R., Moscow, 1985.

Untersteiner, N., On the mass and heat budget of Arctic sea ice, *Arch. Meteorol. Geophys. Bioklimatol., Ser. A*, *12*, 151–182, 1961.

Vowinckel, E., and S. Orvig, The climate of the North Polar Basin, in *Climates of the Polar Regions*, *World Survey of Climatology*, vol. 14, edited by S. Orvig, pp. 129–252, Elsevier, New York, 1970.

Yakovlev, G. N., Thermal balance of the ice cover in the central Arctic (in Russian), *Tr. Arkt. Antarkt. Naucho-Issled. Inst.*, *5*, 33–45, 1958. (Translation available from NTIS as AD-252323.)

Yakovlev, G. N., Snow cover on drifting ice in the central Arctic (in Russian), *Probl. Arkt. Antarkt.*, *3*, 65–76, 1960. (Translation available from the CRREL Library.)

Yanes, A. V., Melting of snow and ice in the central Arctic, *Probl. Arct. Antarct.*, *11*, g-1–g-13, 1962.

Yang, D., et al., Accuracy of Tretyakov precipitation gauge: Result of WMO intercomparison, *Proc. 52nd East. Snow Conf.*, pp. 95–106, Toronto, Ontario, 1995.

Yen, Y.-C., Effective thermal conductivity of ventilated snow, *J. Geophys. Res.*, *67*, 1091–1098, 1962.

E. L. Andreas and R. E. Jordan, U.S. Army Cold Regions Research and Engineering Laboratory, 72 Lyme Road, Hanover, New Hampshire 03755-1290. (rjordan@crrel.usace.army.mil)

A. P. Makshtas, Arctic and Antarctic Research Institute, 38 Bering Street, St. Petersburg, 199397, Russia.

(Received March 23, 1998; revised December 28, 1998; accepted January 4, 1999.)